EXECUTIVE SUMMARY

In ammonia-based thermochemical energy storage (TCES), ammonia is dissociated endothermically as it absorbs solar energy during the daytime. When energy is required, the reverse reaction releases energy to heat a working fluid such as steam, to produce electricity. Ammonia-based TCES has great advantages of simplicity, low cost reactants, and a strong industrial base in the conventional ammonia industry. The concept has been demonstrated over three decades of research at Australian National University, achieving a 24-hour demonstration of a complete system.

At the start of this project, three challenges were identified that would have to be addressed to show that the system is technically and economically viable for incorporation into a CSP plant with an advanced, high temperature power block. All three of these challenges have now been addressed:

1. The ammonia synthesis reaction had not, to our knowledge, been carried out at temperatures consistent with modern power blocks (i.e., ~650°C). The technical feasibility of operating a reactor under high-temperature, near-equilibrium conditions was an unknown, and was therefore a technical risk. The project has successfully demonstrated steam heating to 650°C and energy recovery to steam at the 5 kW_t level.
2. The ammonia system has a relatively low enthalpy of reaction combined with gas phase reactants. This is not a direct disadvantage since the reactants themselves are low cost. The challenge lies in storing the required volume of reactants cost effectively. Therefore, a second key goal was to show, through techno-economic analysis, that underground storage technologies can be used to store the energy-rich gas at a cost that is consistent with the SunShot cost goal. We have identified two promising technologies for gas storage: storage in salt caverns has an estimated cost of \$1/kWh_t and storage in drilled shafts could be on the order of \$7/kWh_t. Together these two options answer the technical challenge associated with storage of gas phase components.
3. While this project is primarily concerned with high-temperature heat recovery and methods to store the gaseous components, it is also important to consider the feasibility of the entire system. Consequently, an additional goal was to perform analysis to show the feasibility of integrating endothermic reactors within a tower receiver. A conceptual design of an ammonia dissociation receiver/reactor has been developed that fits into the same size cylindrical envelope as the molten salt receiver in SAM, and has the same design thermal capacity. The calculated thermal efficiency of this receiver is 94.6%. Thus, this investigation has established the technical feasibility of a surround field tower system using ammonia dissociation.

With these challenges addressed, we proceeded to design a full-scale synthesis and heat recovery system. A model was developed and validated by comparison with our experimental data. A parametric study showed, among other things, the importance of using small tube diameters and spacing to enhance heat transfer. Multi-parameter optimization was used to find a design that minimizes the wall material volume. Finally, cost estimation shows that the ammonia system has good prospects of meeting the Sunshot \$15/kWh_t target: estimated costs of the entire synthesis system for the 220 MW_t plant with 6 hours of storage are \$13/kWh_t using salt cavern storage and \$18/kWh_t

using shaft drilling. Costs per kWh_t are even lower with more hours of storage.

With the established technology of ammonia synthesis as a starting point, the successes of the project have mitigated technical risks associated with high-temperature synthesis reaction, underground storage, and tower receiver design. Estimated costs are less than $15/$kWh_t$ with salt cavern storage. It is now possible to map a time line to commercial deployment that is likely to be shorter and less risky than other thermochemical cycles under active investigation.

UCLA has filed a patent that protects the new ideas developed during this project. Discussions are ongoing with potential investors with the aim of partnering for further work. As well as immediate improvements and extra work with the existing experimental system, a key goal is to extend it to a small solar-driven project at an early opportunity.

TABLE OF CONTENTS

BACKGROUND

The present project on ammonia-based thermochemical energy storage (TCES) for concentrating solar power systems is proceeding in parallel with a range of activities that are investigating other possible thermochemical cycles. Each system has its advantages and challenges.

Perovskite redox cycles are being studied as a potential thermochemical energy storage mechanism. Albrecht et al. [1] developed a thermodynamically consistent modeling approach for these cycles, based on point defect reaction thermodynamics. Their model predicts ideal energy and exergy efficiencies for an energy storage cycle based on strontium-doped calcium manganite of 89% and 63%, respectively. Babiniec et al. [2] are investigating lanthanum-based perovskites; they have synthesized and characterized almost 40 different compositions and extracted thermodynamic parameters for the most promising ones in order to assess their viability as TCES materials. Both of these technologies are in the early stages of development, focusing on physical and thermodynamic properties.

Rönnebro et al. [3] are studying dual-bed metal hydride systems for TCES. Solar energy is stored in an endothermic reaction that releases H_2 from a high-temperature metal hydride. The released H_2 is stored in the creation of a low-temperature metal hydride. The process is reversed to recover energy. Thus far, a high-temperature bed has been demonstrated using titanium hydride.

Melsert and Gangwal [4] are building on earlier efforts to carry out TCES using the reversible carbonation of lime to limestone. They have developed a refined sorbent material that appears to solve earlier challenges with the sorbent degrading over time. In preliminary testing, their new material has shown high CO_2 uptake that has not degraded over 100 cycles. Rhodes et al. [5] are working on a strontium carbonate-based carbonation cycle and addressing the same issues with decreasing energy absorption over time; they have identified the mechanism to be slowing carbonation kinetics.

As described above, the bulk of the present TCES work involves gas-solid reactions, in contrast to the ammonia system that involves only fluid phase reactants. Gas-solid reactions often offer higher enthalpy of reaction, but must deal with the heat and mass transfer challenges that come with a solid reactant. Furthermore, these other storage concepts, while promising, are not as far developed as ammonia-based TCES.

Ammonia-based TCES can build on the extensive industrial experience with ammonia synthesis. The reaction has been well-studied and an array of catalysts has been developed. Most ammonia plants use natural gas as feedstock. In this context, the most expensive step is separating H_2 from natural gas and naturally that has received the most emphasis. Consequently, according to [6], remarkably little innovation has occurred with respect to ammonia converter designs.

Recently, as reviewed in [7], a few papers on ammonia synthesis or dissociation have noted the enhanced heat and mass transfer associated with small physical scales. However, there does not appear to have been any systematic quantification of the benefit either experimentally or through modeling. A number of papers, such as [8-10],

have discussed optimization of ammonia synthesis reactors, with the design variables including the inlet temperature, reactor length, counterflow vs. parallel flow design, etc. However none of these has considered changes to the lateral dimensions, e.g. tube diameters and spacing. Thus, it appears that our work (described in this report) to optimize ammonia synthesis in part by using smaller lateral dimensions is relevant and fills a gap in the literature.

INTRODUCTION

In ammonia-based thermo-chemical energy storage (TCES), see Figure 1, ammonia is dissociated endothermically (NH_3 + 66.8 kJ/mol $\rightleftharpoons$ 1/2 N_2 + 3/2 H_2) as it absorbs solar energy during the daytime. The products of reaction are stored. When energy is required, the reverse reaction releases energy to heat a working fluid such as steam, to produce electricity. Ammonia-based TCES has great advantages of simplicity, low cost reactants, and a strong industrial base in the conventional ammonia industry. The concept has been demonstrated over three decades of research at Australian National University (ANU), achieving a 24-hour demonstration of a complete system, with dish receiver, endothermic and exothermic reactors, and storage vessel [11].

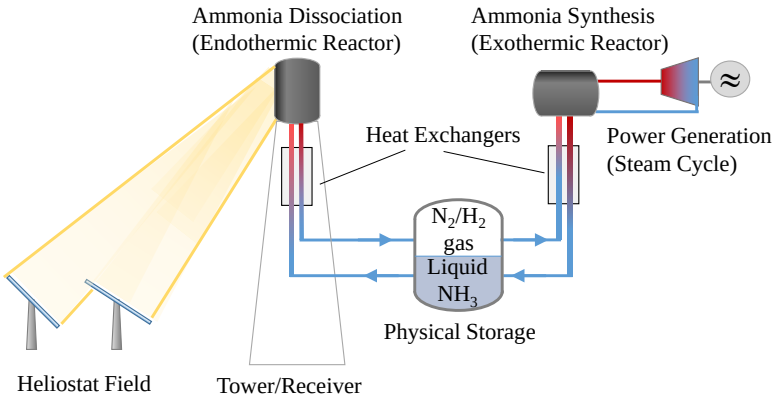

Figure 1: Schematic of ammonia-based thermochemical energy storage.

At the start of this project, three challenges were identified that would have to be addressed to show that the system is technically and economically viable for incorporation into a CSP plant with an advanced, high temperature power block:

1. The ammonia synthesis reaction had not, to our knowledge, been carried out at temperatures consistent with modern power blocks (i.e., ~650°C). The technical feasibility of operating a reactor under high-temperature, near-equilibrium conditions was an unknown, and was therefore a technical risk.
2. The ammonia system has a relatively low enthalpy of reaction combined with gas phase reactants. This is not a direct disadvantage since the reactants themselves are low cost. The challenge lies in storing the required volume of reactants cost effectively. Therefore, a second key goal was to show, through techno-economic analysis, that underground storage technologies can be used to store the energy-rich gas at a cost that is consistent with the SunShot cost goal.
3. While this project is primarily concerned with high-temperature heat recovery and methods to store the gaseous components, it is also important to consider the feasibility of the entire system. Consequently, an additional goal was to perform analysis to show the feasibility of integrating endothermic reactors within a tower receiver.

To address the three challenges described in the above paragraphs, the project was organized into various tasks:

- Task 1.1 and aspects of 5.1 and 5.2 pertained to developing a model, validating it using experimental data, and using the model to design synthesis reactors for heating supercritical steam. Early in the project, modeling (and experiments) showed that ammonia synthesis could indeed be used to heat supercritical steam to 650°C. The model was subsequently validated by comparison with our experimental data and was used to design our 5 kW_t system. The model was also used to explore system behavior in preparation for system optimization (Task 6.1). A parametric study showed the importance of using small tube diameters to enhance heat transfer.
- The objective of Tasks 2.2, 2.3, 2.3R, and aspects of 5.1 and 5.2 was to generate experimental data to validate the model and also to experimentally demonstrate the use of ammonia synthesis to heat 26 MPa supercritical steam from 350°C to 650°C, at a power level of 5 kW_t by the end of the project. The project has successfully demonstrated steam heating to 650°C and energy recovery to steam at the 5 kW_t level.
- The goal of Tasks 2.1 and 5.3 was to conduct preliminary lifetime testing of catalyst performance at 650°C. The results of this testing have shown some anomalies, but a more controlled testing protocol would be required to fully understand their causes. If iron-based catalyst is unsuitable at the elevated system temperatures, another catalyst such as iron-cobalt should be used.
- Task 3.1 tested the hypothesis that some form of underground storage can provide a technically and economically viable option for containment of gas phase components. At the end of the project there are two particularly promising underground storage approaches for storing the gas mixture: solution mined salt caverns and large diameter shaft drilling. Salt caverns offer storage costs that could be as low as \$1/kWh_t. Shaft drilling offers a more expensive but more universally applicable solution with costs on the order of \$7/kWh_t. Together these two options answer the technical challenge associated with storage of gas phase components.
- The purpose of Task 4.1 was to analyze options for coupling endothermic ammonia dissociation reactors to a tower receiver. A conceptual design of an ammonia dissociation receiver/reactor has been developed. This receiver fits into the same size cylindrical envelope as the molten salt receiver in SAM, and has the same design thermal capacity. The calculated thermal efficiency of this receiver is 94.6%. Thus, this investigation has established that a surround field tower system based on ammonia dissociation reactor tubes is technically feasible.
- The purpose of Task 6.1 was to optimize the design of a synthesis reactor system for a full-scale power plant (220 MW_t with 6 hours of storage) and perform a cost-estimate to show that the Sunshot goal of \$15/kWh_t could be met. Multi-parameter optimization was used to find a design that minimizes the wall material volume. Smaller tube diameters are key and the smallest readily available tube sizes were selected; performance could be improved even further with smaller lateral dimensions. Finally, cost estimation shows that the ammonia system has good prospects of meeting the Sunshot target: estimated costs of the entire synthesis system for the 220 MW_t plant with 6 hours of storage are \$13/kWh_t using salt cavern

storage and \$18/kWh$_t$ using shaft drilling. Costs per kWh$_t$ are even lower with more hours of storage.

The status of Final Deliverables is listed below. Each accomplishment will be discussed in detail in the Project Results and Discussion.

FD-1. A validated, high-fidelity model of a synthesis reactor system will be completed. The model will predict steam outlet temperature and thermal power output and will elucidate the relationship between input variables (gas pressure, flow rate, and incoming composition; steam pressure, flow rate, and inlet temperature; reactor geometry and catalyst) and output variables (steam outlet temperature and thermal power output). **COMPLETE**

FD-2. A synthesis reactor and integral gas-to-steam heat exchanger system will be constructed and tested that heats 2.5 g/s of steam from 350°C to 650°C, corresponding to thermal power output of 5 kW$_t$, under steady-state conditions. **COMPLETE**

FD-3. The experimentally validated model, along with optimization tools, will be used to define specific design modifications and operating conditions that would allow scale-up to 220 MW$_t$ plant operation with steam heated from 350°C to 650°C at ~26 MPa, requiring a steam mass flow rate of 110 kg/s. **COMPLETE**

FD-4. Underground storage options will be identified and ranked on the basis of cost per unit of energy stored and other criteria. **COMPLETE**

FD-5. The combined cost for underground storage and structural materials and catalyst for the synthesis reactor system will meet the goal of ≤ \$15/kWh$_t$. **COMPLETE**

FD-6. A model for the endothermic reactor/receiver will show a receiver energy efficiency ≥ 90%. **COMPLETE**

FD-7. A tech-transfer package will be prepared summarizing the results of modeling, experiments, and cost estimation, for the purpose of engaging an industry partner in a next step effort. **COMPLETE (THIS REPORT)**

PROJECT RESULTS AND DISCUSSION

Model and Parametric Study (Task 1.1)

The Model

One of the first tasks of the project was to develop a model of the synthesis reactor (also referred to in this report as the “heat recovery reactor,” since this is where the synthesis reaction is used to heat supercritical steam). A pseudo-homogeneous steady-state model originally developed by Richardson et al. [12] is used to simulate the reaction kinetics and thermodynamics of reacting gas in the catalytic bed. The model has been modified and validated by Lovegrove and others at ANU for ammonia dissociation and synthesis [13,14]. Chen et al. [15] have further improved the model with the capability of simulating heat transfer between the reaction in the bed and a secondary fluid. In this model, the catalyst bed is treated as a continuum with averaged properties, i.e. effective conductivity (k_{eff}) and effective diffusivity (D_{eff}) [12]. Figure 2 shows a schematic of a typical tube-in-tube reactor. Synthesis gas (stoichiometric N_2+3H_2, referred to as “gas” for simplicity) flows through a catalyst bed in the annulus and reacts exothermically. A secondary fluid (steam in Figure 2) is in counterflow in the inner tube, and is heated by the reacting gas. In our work, the secondary fluid is either

supercritical steam (in the heat recovery reactor) or synthesis gas being preheated (in the autothermal reactor to be discussed later).

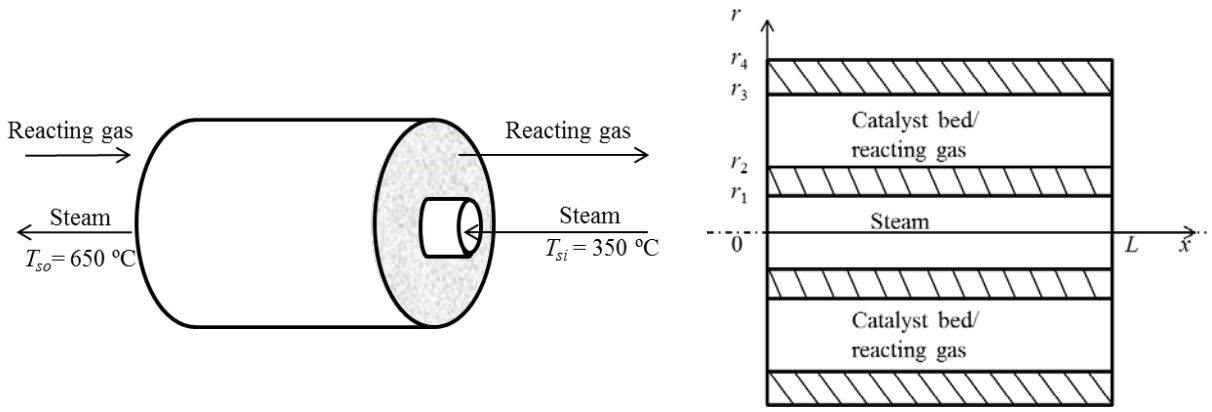

Figure 2: Schematic of a synthesis reactor.

The energy conservation equations for the reacting gas and secondary fluid (radially lumped) can be expressed as:

$$\rho_g v_g C_{p,g} \frac{\partial T_g}{\partial x} = \frac{1}{r}\frac{\partial}{\partial r}\left(k_{eff} r \frac{\partial T_g}{\partial r} \right) + \dot{r}''' \Delta H \tag{1}$$

$$\dot{m}_s C_{p,s} \frac{dT_s}{dx} = 2\pi r_1 q_w'', \text{ where } q_w'' = U\left[T_g(r = r_2, x) - T_s(x) \right] \tag{2,3}$$

The governing equation for mass species conservation is:

$$\rho_g v_g \frac{\partial f_{NH3}}{\partial x} = \rho_g D_{eff} \frac{1}{r}\frac{\partial}{\partial r}\left(r \frac{\partial f_{NH3}}{\partial r} \right) + \dot{r}''' \tag{4}$$

In Equations (1)-(4), ρ_g, v_g, and $C_{p,g}$ are the density, superficial velocity, and specific heat of the gas, $\dot{m}_s$ and $C_{p,s}$ are the mass flow rate and specific heat of the secondary fluid, T_g is the gas temperature, T_s is the secondary fluid temperature, f_{NH3} is the ammonia mass fraction, k_{eff} and D_{eff} are the effective thermal conductivity and effective diffusivity of the gas/catalyst bed, $\dot{r}'''$ is the ammonia reaction rate (kg/m^3·s), ΔH is the heat of reaction (J/kg), and U is a conductance that accounts for the inner tube wall and heat transfer coefficient in the secondary fluid.

The chemical reaction rate is modeled using the Temkin-Pyzhev rate equation [16]:

$$\dot{r}''' = \eta k_{o,m} \exp\left(\frac{-E_a}{R_u T} \right) \left[K_p^{-1} P_{N2} \left(\frac{P_{H2}^3}{P_{NH3}^2} \right)^{\alpha} P_o^{-(1+\alpha)} - \left(\frac{P_{NH3}^2}{P_{H2}^3} \right)^{1-\alpha} P_o^{1-\alpha} \right] \tag{5}$$

Here, P_o is the standard state pressure of 1 atm, explicitly included to make the dimensions consistent, P_i are the partial pressures of the constituents, K_p is the equilibrium constant, α is an empirical parameter, E_a is the activation energy, $k_{o,m}$ is the pre-exponential constant (in kg/m^3·s), and η is the nondimensional effectiveness factor

which accounts for mass diffusion within the catalyst particle [12,17-19]. Note that a system pressure of 30 MPa was selected based on considerations of experience at ANU, industrial practice, and initial modeling.

Total pressure is assumed constant throughout the reactor for purposes of calculating thermodynamic properties, partial pressures, etc. However, the pressure drop is an important consideration and is calculated using the Ergun equation:

$$\Delta p = \frac{150\mu_g L}{D_p^2}\frac{(1-\varepsilon)^2}{\varepsilon^3}v_g + \frac{1.75L\rho_g}{D_p}\frac{(1-\varepsilon)}{\varepsilon^3}v_g^2 \quad (6)$$

where μ_g is the gas viscosity, L is the reactor length, D_p is the catalyst particle equivalent diameter, and ε is the bed porosity.

Typical Model Results and Parametric Study of Synthesis/Heat Recovery Reactor

At the onset of the project, it was not known whether it was possible to achieve synthesis temperatures high enough to heat steam to 650°C. It quickly became apparent, through modeling and experiments, that it was indeed possible. At that point, one major objective became optimizing the synthesis system for low cost. A rough cost estimate clearly showed that the wall material (whether Inconel or steel) was significantly more expensive than the catalyst or initial ammonia loading. Therefore, one goal was to minimize the wall material volume of the entire synthesis system. Eventually this led to a multi-parameter optimization problem (Task 6.1) which will be discussed later in this report. First, however, it is instructive to consider typical model results and a parametric study of the synthesis/heat recovery reactor to understand trends that lead to lower volume.

As shown previously in Figure 2, the reactor configuration is tube-in-tube with synthesis gas reacting in the catalyst bed and supercritical steam in counterflow in the inner tube. The opposite configuration was also studied, with steam in the annulus, but was found to require larger material volumes.

High temperature creep-resistant nickel alloy material, i.e. Inconel 625, was selected for the tube wall. A wall thickness factor F can be defined as the ratio of wall thickness over inner diameter of the tube. Based on the ASME Boiler and Pressure Vessel Code [20], the allowable stress of Inconel at 700°C for a 200,000-hour life, and an assumed operating pressure of 30 MPa, the wall thickness factor F is 0.46. Thus the wall thickness can be related to the tube diameters according to:

$$F = \frac{r_2 - r_1}{2r_1} = \frac{r_4 - r_3}{2r_3} = 0.46 \quad (7)$$

If this yields a wall thickness less than 0.05 cm, the wall thickness is taken to be 0.05 cm as a realistic minimum.

The steam enters at 350°C (slightly subcritical; T_c = 373.9°C) and is to be heated to 650°C. The gas enters the reactor after having been preheated using a combination of recuperating heat exchanger and autothermal reactor. These “preconditioning” components will be studied in the multi-parameter optimization task, but for now we simply assume that the gas enters at a specified temperature as pure synthesis gas.

Once input conditions of tube diameters, gas and steam mass flow rates, and inlet gas conditions (temperature and ammonia mass fraction) are set, the model calculates the temperature and mass fraction distributions, and establishes the required reactor length for the steam to be heated from 350°C to 650°C.

Figure 3(a) shows an example of the bulk (cross-sectional average) temperature distribution of gas (green) and steam (red) along the *x*-direction (the direction of gas flow through the reactor). The conditions are given in the figure caption. As soon as the gas enters the reactor (at $x = 0$), it undergoes a rapid temperature increase because of the high reaction rate caused by the elevated temperature. The temperature increase brings the gas close to equilibrium conditions and the reaction slows, but does not cease. Thereafter, the temperature of the reacting gas decreases along the reactor length as it loses heat to the steam. The steam enters at the right at 350°C and exits at the left at 650°C (by design). The slope change in the region around T_{pc} = 389°C corresponds to the pseudocritical regime of the steam, with very large specific heat.

Figure 3(b) shows an example of the ammonia mass fraction distribution. The solid curve is the mass fraction of ammonia in the gas stream as it flows through the reactor. The dashed curve is the equilibrium mass fraction corresponding to the bulk reactor temperature at each axial location. The ammonia mass fraction quickly reaches equilibrium near the reactor inlet and then increases more gradually as the reaction rate slows (due to lower temperature). Further downstream the mass fraction deviates from the equilibrium curve as the reaction rate is no longer fast enough to maintain near-equilibrium conditions.

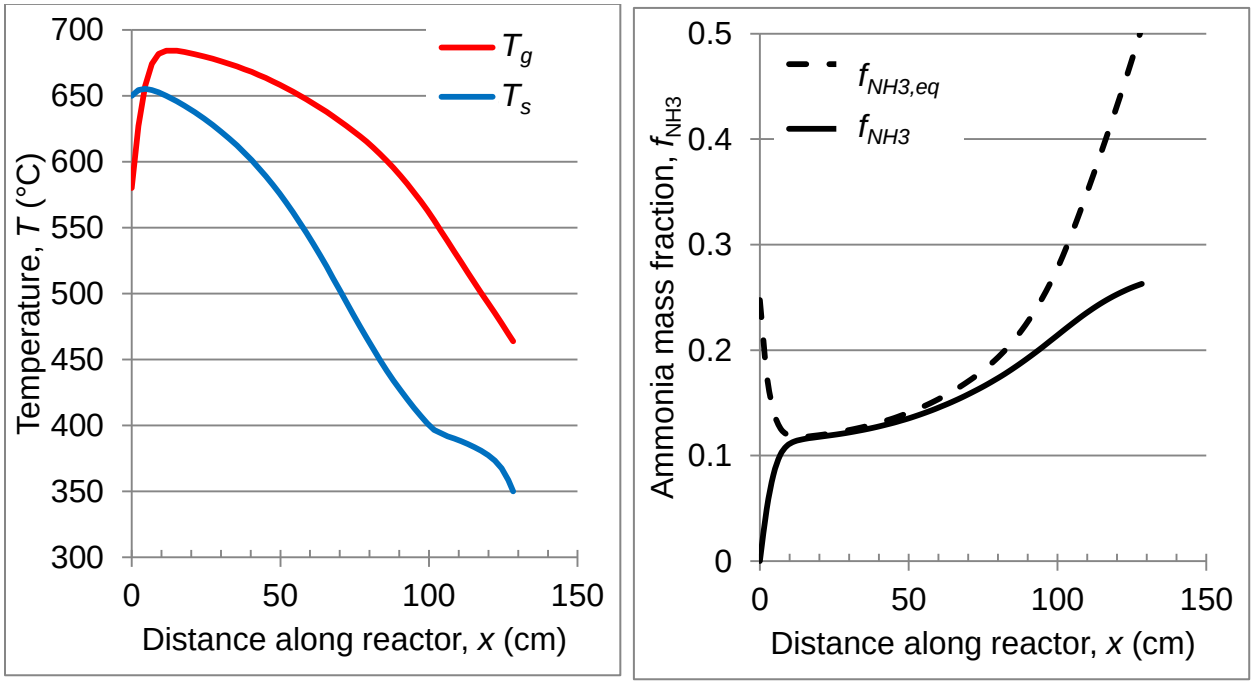

(a) (b)

Figure 3: An example of (a) temperature and (b) ammonia mass fraction distributions in the synthesis reactor. Conditions are D_2 = 0.5 cm, D_3=1.0 cm, $\dot{m}_g$ = 1.6 g/s, $\dot{m}_s$ = 1.0 g/s, $T_{g,in}$ = 580°C, and $f_{NH3,in}$ = 0.

Basically, the synthesis reactor can be viewed as a counter flow heat exchanger with the hot stream reacting exothermically. Similar to a heat exchanger, parameters such as inlet temperatures, diameters, and mass flow rates affect the required reactor length and volume. A parametric study has been conducted to investigate the effects of those parameters on the usage of tube wall material. We report on the effect of two parameter groupings that have important consequences, namely the tube diameters and the two mass flow rates.

Diameters: For the tube-in-tube configuration, the heat transfer process is strongly influenced by the diameters of inner and outer tubes. In order to investigate the effect of diameters on the required wall volume, D_2 was varied from 1 to 1.3 cm and D_3 was varied in the range 0.4-0.7 cm. Other conditions are given in the caption of Figure 4. Figure 4(a) shows the required reactor wall volume as a function of the diameters. It can be seen that the smallest reactor wall volume occurs when both D_2 and D_3 are smallest. This is because heat transfer for both gas and steam is improved by making the diameters smaller. Figure 4(b) shows the pressure drop in the catalyst bed as a function of diameters; the maximum pressure drop occurs when D_2 is maximum and D_3 is minimum, which corresponds to the minimum cross sectional area of the catalytic bed. Thus one important lesson is that heat transfer is improved and wall volume is decreased by reducing tube diameters, but there can be a detrimental impact on pressure drop. Within the optimization study reported later, a constraint will be imposed on the allowable pressure drop. Note that the pressure drop in the steam tube is three orders of magnitude smaller, only 1.1 kPa.

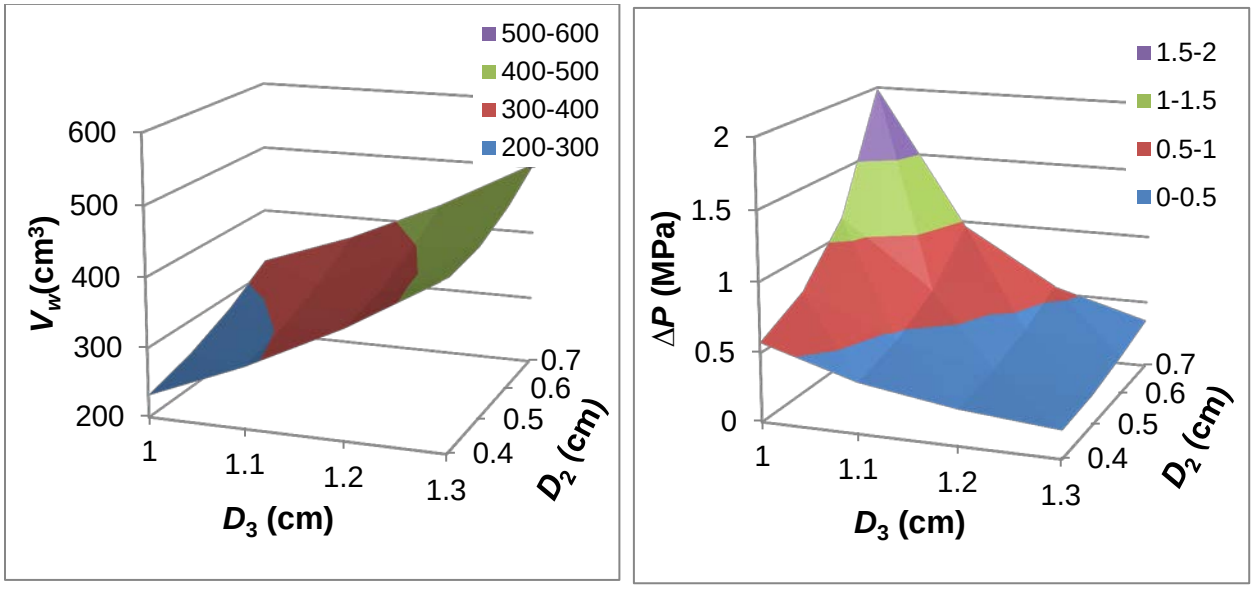

(a) (b)

Figure 4: (a) Required wall volume and (b) pressure drop in catalyst bed as functions of diameters. Conditions are: $\dot{m}_g$ = 1.6 g/s, $\dot{m}_s$ = 1.0 g/s, $T_{g,in}$ = 600°C, and $f_{NH3,in}$ = 0.

We also looked at the issue of tube dimension in another way. We investigated the effect of scaling diameters down by a factor of 10 (from D_2 = 3 cm to 0.3 cm), while simultaneously optimizing mass flow rates (not holding them fixed). For the smaller diameter, the number of tubes must then be increased to heat the same steam flow rate.

Because of the vastly improved heat transfer for smaller diameters, each tube can be shorter by about a factor of 10 to achieve the prescribed steam temperature increase. While more tubes are needed, the reduction in diameter, wall thickness, and length results in a dramatic reduction in wall and catalyst volumes by more than 70 times.

Mass flow rates: The mass flow rates of hot and cold streams in a heat exchanger are important factors affecting the required heat exchanger size. Similarly, the gas and steam mass flow rates affect the synthesis reactor volume. The steam mass flow rate was varied from 0.6 to 1.3 g/s, and the gas mass flow rate from 1.6 to 2.3 g/s, while the diameters and inlet temperature were held fixed (see conditions in Figure 5 caption). The reactor length needed to heat steam from 350 to 650°C was determined, along with the corresponding reactor wall volume. In order to fairly compare the results, Figure 5(a) shows the required wall volume *normalized by the power delivered to the steam*. The required volume per unit power is maximized when both of the mass flow rates are at their maxima. The pressure drop within the catalyst bed is also shown in Figure 5(b), and is maximized when the flow rates are maximized. Since the required pumping power is proportional to mass flow rate and pressure drop, at some point saving reactor wall volume by increasing mass flow rates is not worthwhile. This trade-off is addressed later in the optimization task by setting a constraint on the pumping power.

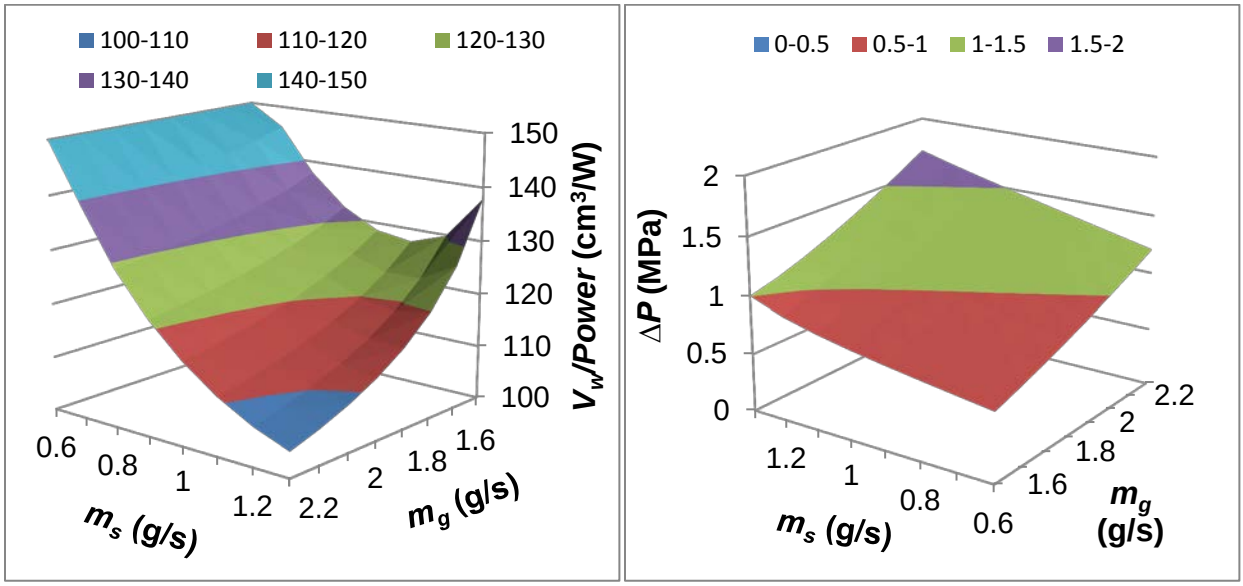

(a) (b)

Figure 5: (a) Required reactor wall volume per unit power and (b) catalyst bed pressure drop as functions of gas and steam flow rates. Conditions are D_2 = 0.5 cm, D_3=1.0 cm, $T_{g,in}$ = 580°C, and $f_{NH3,in}$ = 0.

Adiabatic Reactor Concept: Using the model to explore the reactor behavior led to an additional observation. Referring back to Figure 3, it can be seen that as the steam (red curve) travels from right to left, it reaches a peak and then slightly decreases in temperature as it *loses* heat to the cooler gas near the inlet. Under some circumstances this effect can be more pronounced. It makes sense, therefore, for the steam to exit the reactor at its peak temperature. Another way of saying the same thing is that the gas can be allowed to react in an adiabatic reactor before it enters the heat recovery reactor

where it exchanges heat with the steam. This has an additional benefit with respect to pressure drop. We know that tube diameters should be small in the heat recovery reactor to enhance heat transfer. However, in an adiabatic reactor there is no benefit to smaller tubes. In fact, it can be shown that for a given mass flow rate of gas, a certain *volume* of catalyst is required for the gas to reach equilibrium conditions, regardless of whether the reactor is long and thin or short and fat. Furthermore, the reactor wall volume is proportional to the catalyst volume (because of the requirement that wall thickness scales with diameter). Therefore, for a certain required adiabatic reactor volume, the pressure drop can be reduced by making the reactor short and fat. This concept informs the later optimization study.

Model Improvement and Validation (Tasks 5.1 and 5.2)

Over the course of the project, we ran a series of experiments designed to characterize the fundamental behavior of synthesis/heat recovery reactors in order to improve and validate our model. The experimental set-up and ultimate experimental results are described in a later section. In this section we will summarize the validation efforts and show sample comparisons between experiments and model predictions. These experiments were carried out in the “intermediate scale” reactor. The geometry of that reactor is as shown schematically in Figure 2, with D_1 = 0.39 cm, D_2 = 0.64 cm, D_3=1.88 cm, and D_4 = 2.67 cm. The reactor length was 1.1 m.

Rate Parameter Experiments

We first ran experiments for the purpose of extracting reaction rate parameters. In these experiments there was no steam running through the reactor, only synthesis gas flowing through the catalyst bed. The outer reactor wall was well insulated so that conditions were as close to adiabatic as possible. Conceptually, an adiabatic reactor is suitable for determining rate parameters because it removes heat transfer effects. The initial rate of temperature rise at the reactor inlet is then a direct manifestation of the reaction rate, and can therefore be used to infer the rate parameters. Of course, heat losses can never be entirely eliminated, so they were estimated based on experimental measurements and included in our data analysis.

We ran a set of experiments with different gas flow rates and inlet temperatures. For each test, the reaction rate was inferred from the initial rate of temperature rise (corrected for heat loss). Then we sought the values of activation energy (E_a) and pre-exponential constant (k_o) in the Tempkin-Pyzhev rate equation that minimized the error between experimental and predicted reaction rates. Unfortunately, we found that this procedure could not accurately determine E_a and k_o *independently*. Thus we selected the same pre-exponential constant as in the work of Kreetz and Lovegrove [13], $k_o = 1.1 \times 10^{11}$ mol/cm^3-s, and found the value of E_a that provided the best fit to our experimental reaction rates, namely E_a = 215 kJ/mol. This E_a value is reasonably close to the value of E_a = 200 kJ/mol found by Kreetz and Lovegrove for an iron-based catalyst (not the exact same product as what we used).

The ultimate test of the rate parameters is how well they predict the reactor behavior in the conditions of interest of this project, namely when steam is heated in a synthesis reactor. We will show comparisons later.

Supercritical Steam Heat Transfer Experiments

When steam is heated from 350°C to 650°C at 26 MPa, it traverses the pseudo-critical line at 389°C. In this vicinity, properties vary dramatically with temperature. Standard heat transfer correlations for the Nusselt number as a function of the Reynolds and Prandtl numbers do not properly account for these large variations. There is a significant body of literature on heat transfer in supercritical steam, e.g. [21,22], but the behavior can depend strongly on details that may vary from one system to another, for example, the magnitude of natural convection effects. Therefore, we undertook our own experimental investigation of heat transfer in supercritical steam flow for the same conditions as in our reactor, and compared our results to correlations from the literature.

Specifically, we built a test apparatus in which steam enters at the bottom of a vertical tube and runs upwards. The tube is identical to the inner tube through which steam flows in our reactor, with inner and outer diameters of 0.39 mm and 0.64 mm. The tube is heated using nozzle heaters encircling the outer wall. The inlet, outlet, and wall temperatures are measured. From knowledge of the input power, we can determine the bulk temperature, T_b, at any axial location. Then the local heat transfer coefficient can be found from its definition, $h = q'' / (T_w - T_b)$, where q'' is the heat flux (input power divided by surface area) and T_w is the measured wall temperature.

We will now compare our measured heat transfer coefficients to the correlations of Jackson [21] and Mokry [22] for supercritical steam and with the standard Dittus-Boelter correlation, all of which are for turbulent flow. Results are shown for an illustrative case that spans the pseudocritical temperature, T_{pc} = 389°C (at 26 MPa). The comparison is shown in Figure 6. The heat transfer coefficient is presented as a function of steam bulk temperature; since the fluid is heating up as it travels through the tube, the bulk temperature also roughly represents distance from the tube inlet.

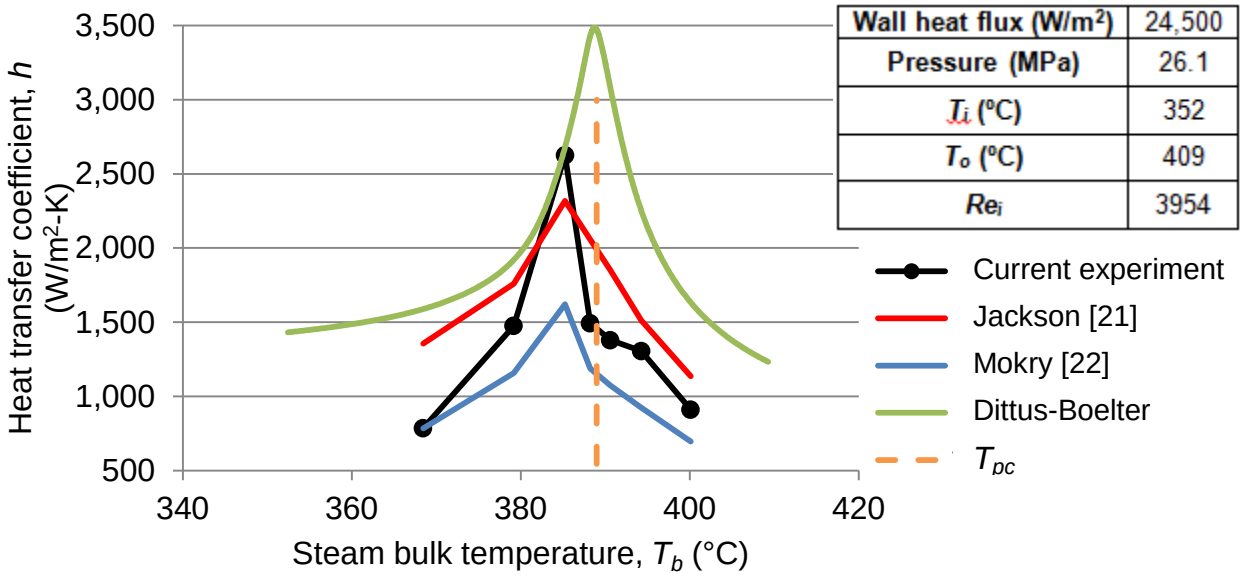

Figure 6: Heat transfer coefficient comparison for supercritical steam flow.

There is a peak in the experimental heat transfer coefficient and in the Jackson and Mokry correlations slightly before the pseudocritical temperature, caused by the wall temperature reaching the pseudocritical temperature before the bulk temperature does. On the other hand, the heat transfer coefficient predicted by the Dittus-Boelter correlation reaches its peak exactly at the pseudocritical temperature and does not accurately reflect the experimental behavior. Overall, the root mean square error between our experimental results and Jackson's correlation is the smallest of the three correlations. Therefore we will use Jackson's correlation in our reactor model to simulate heat transfer in the steam flow. We have chosen not to create our own correlation because we think the Jackson results are more thoroughly established than ours.

Steam Heating Experiments to Validate Model

We exercised the aforementioned intermediate scale reactor to demonstrate that the model can capture the integrated behavior of reaction, packed bed heat transfer, and supercritical steam heat transfer. First, in order to improve steam heat transfer, we inserted a third tube within the inner tube (see Figure 7) so that the steam channel is a narrow annulus—the gap is 0.34 mm. By decreasing the lateral dimension of the steam channel, the steam heat transfer coefficient is increased.

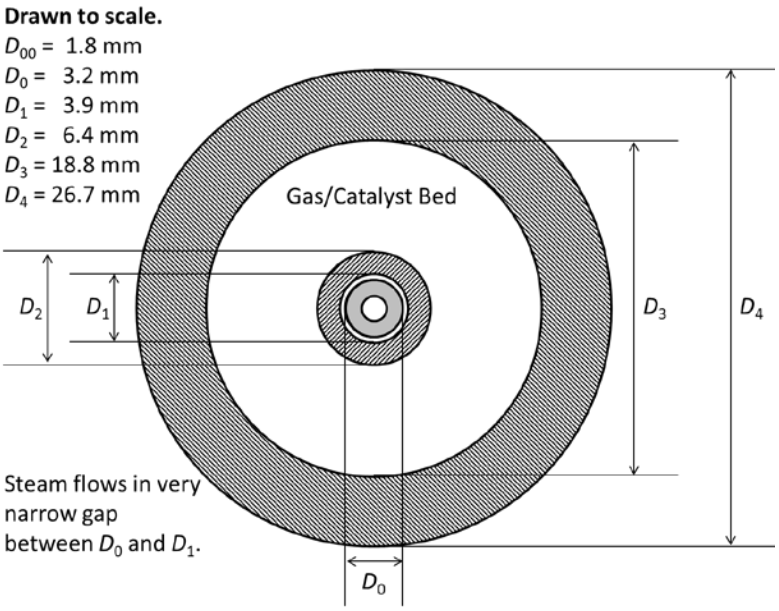

Figure 7: Reactor cross-sectional geometry. The smaller tube with outer diameter D_0 was inserted inside the steam tube to both enhance heat transfer within the steam and enable insertion of thermocouples to measure the inner wall temperature (essentially the steam temperature).

We present here one example of gas and steam temperature distributions in the reactor, for the case of maximum power with the intermediate scale reactor. Figure 8 presents the outer wall and inner wall temperature profiles for experiments and model predictions. Focusing first on the experimental measurements (data points), the outer wall temperature ($T_{o,exp}$) was measured with thermocouples attached to the outer wall of the catalyst bed and can be thought of as representing the gas temperature. The steam

temperature ($T_{s,exp}$) was measured by inserting a moveable thermocouple into the inner tube of diameter D_0. It was not possible to measure the steam temperature along the entire reactor length. The steam inlet temperature (the point at x = 110 cm and ~350°C) was measured with a separate thermocouple permanently positioned in the steam tube at its inlet. The gas flows from left to right, experiencing a rapid temperature increase of around 50°C near the inlet. The steam flows from right to left, exiting at a temperature within around 15°C of the peak gas temperature.

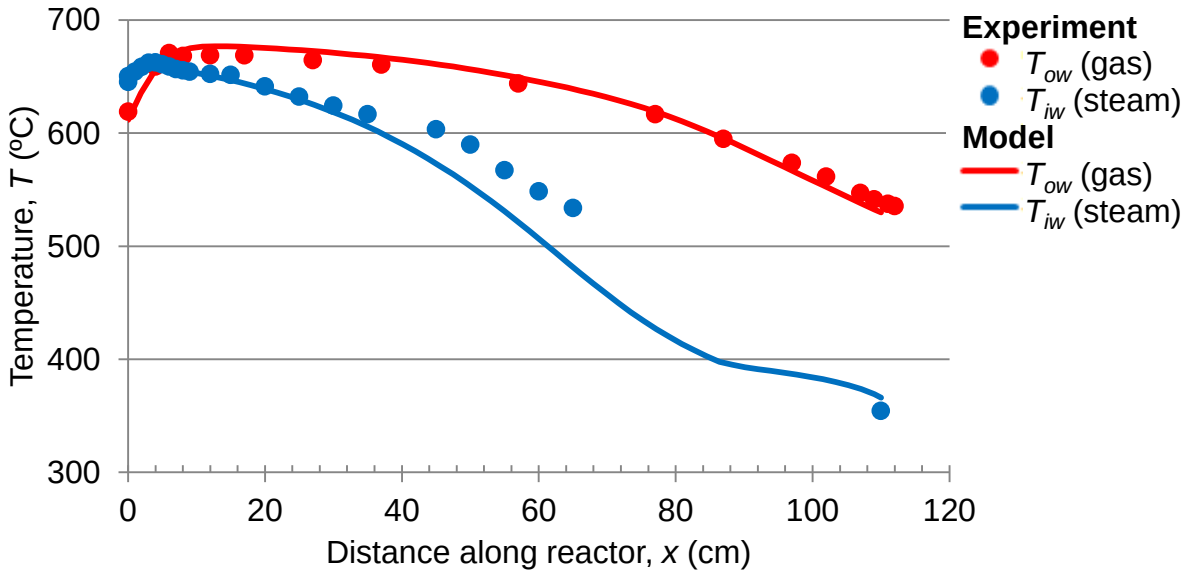

Figure 8: Comparison between experimental and predicted outer wall (gas) and inner wall (steam) temperatures. Case 04/29, 14:00.

Turning next to the agreement between the experimental and model results (the latter shown with solid curves), it can be seen that the outer wall temperature matches very well over the entire reactor length, as does the steam temperature measured with the moveable thermocouple from x = 0 to around x = 30 cm. Beyond that location the agreement starts to deviate. It appears that the model may be under-predicting the heat transfer in that region. The agreement is also very good for the steam inlet temperature at x = 110 cm (note that the model marches from left to right with respect to the figure, therefore steam *outlet* temperature is a model input and steam *inlet* temperature is predicted). Since the inlet steam temperature is predicted very closely, the power added to the steam is also accurately predicted. In this case, 1.8 kW_t is added to the steam.

The ultimate test of the model is how well it works in predicting the temperature of steam being heated in the reactor and the corresponding power delivered to the steam. With reference to Figure 8 and a set of similar comparisons for different runs, we conclude that the model can be used with confidence to predict reactor performance.

Experimental Work (Tasks 2.1, 2.2, 2.3R, 5.1, 5.2, and 5.3)

Experimental Setup

The experimental system has evolved over the course of the project. In work reported earlier, we used a single dissociation reactor and a single synthesis reactor (the intermediate scale reactor). This arrangement was used for model validation, as

described previously. In the final stage of our project, we have built and operated a closed loop 5 kW_t scale ammonia synthesis system. The system can be divided into three sub-systems: dissociation, synthesis/heat recovery, and steam generation (Figure 9). The closed loop system cycles between dissociation and synthesis, with a storage tank in between, as would occur in a full scale energy storage system. As will be shown below, the current peak operating capacity has been measured as 5.2 kW_t and the autothermal capacity has been established as 845 W_t. With additional modifications and testing, it is believed even greater capacities can be reached.

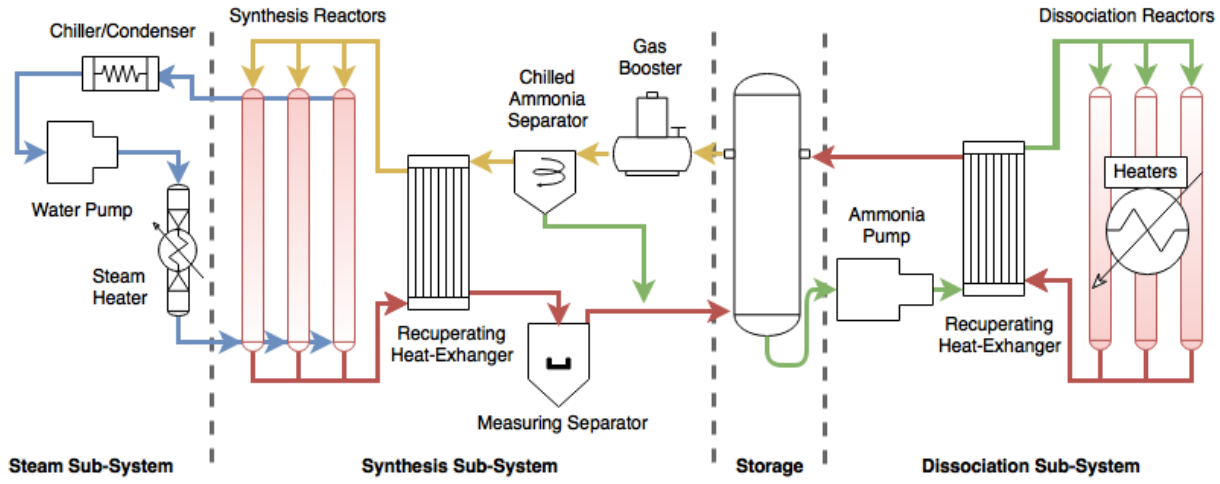

Figure 9: Schematic of the closed loop ammonia synthesis system.

Our research has pointed in the direction of smaller tube diameters being a more cost-effective design approach. Consequently, scaling up to a full-scale system would not mean using larger tube diameters, but rather using more tubes. We therefore decided that in designing the 5 kW_t system, we would use the same diameter tubes we had been using for smaller systems (see Figure 7), but use multiple tubes.

Dissociation: The purpose of the dissociation subsystem is to generate synthesis gas (N_2 + $3H_2$) for the synthesis/heat recovery reactor. At the heart of the dissociation sub-system are three 1.8 m long, 27 mm OD dissociation reactors constructed from Inconel 625. The dissociators employ iron-based catalyst and external wall heaters for their heat source (replacing solar energy). Ammonia (coming from storage) is fed into the dissociation subsystem via an air-actuated liquid booster, MaxPro LSF150. The synthesis gas-rich mixture exiting the dissociation system enters storage.

Synthesis/Heat Recovery: The synthesis/heat recovery subsystem consists of three 1.8 m long synthesis reactors with steam running through a center tube as shown previously in Figure 7. The catalyst is iron-based, ground to particle diameters in the range 0.4 to 0.6 mm. A Hydraulics International gas booster, 5G-DS, drives the synthesis gas through the system. A high pressure Coriolis flow meter, Emerson CMF010P, measures the flow rate. The gas booster draws synthesis gas from the top of a chilled ammonia separator. The separator removes saturated ammonia from the gas supply coming from storage in order to provide a purer, more reactive feedstock for the

synthesis reactors. The use of a recuperating heat exchanger serves to preheat the incoming synthesis gas using the synthesis reactor exhaust stream.

The three identical synthesis reactors each have the capability of operating independently from one another as well as in three different modes (see Figure 10, where the synthesis gas indicated at the top is coming from the recuperating heat exchanger). The first mode (Mode A, Figure 10(a)) has the incoming synthesis gas pre-heated through a combination of recuperating heat exchanger and electric heaters, in the same manner that the previous intermediate scale reactor operated. This enabled accurate and stable control of the inlet conditions for the purposes of establishing maximum steam heating capacity.

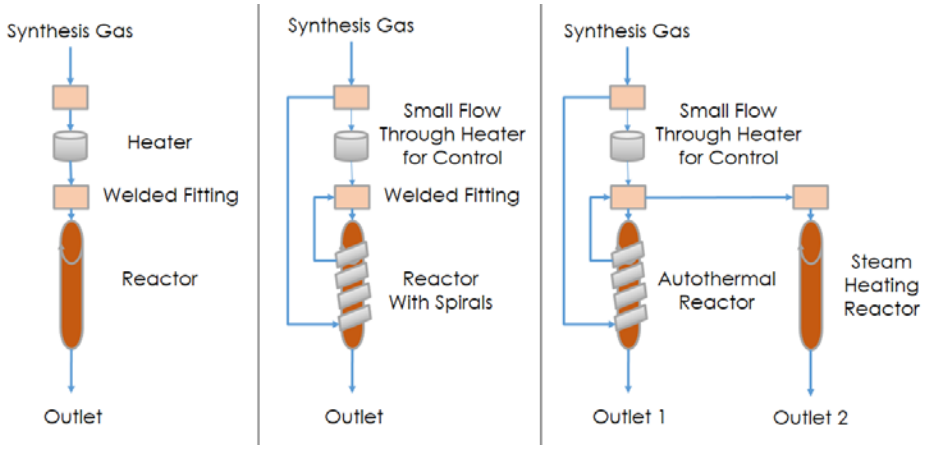

(a) (b) (c)

Figure 10: Three operating modes of the 5 kW_t synthesis reactor system.

The second mode of operation (Mode B, Figure 10(b)) diverts a portion of the incoming synthesis gas coming from the recuperator and passes it through outer spirals affixed to the surfaces of the reactors. The actual reactors with outer spirals are shown in Figure 11 (next page). The gas is then fed back into the reactor so that the heat of reaction simultaneously heats the synthesis gas in the outer spiral and the steam in the inner tube. (Electrical heating of a portion of the synthesis gas stream is enabled to assure fine control of conditions if needed.)

The third mode of operation (Mode C, Figure 10(c)) is similar to the second mode in that the synthesis gas is preheated using autothermal reactors. In the third mode of operation, two reactors are used solely as autothermal reactors to preheat the gas for the third reactor which is solely responsible for steam heating (in Figure 10(c) the reactor on the left is one of two reactors that feed the steam heating reactor on the right). By splitting up the roles of preheating and steam heating, we are able to investigate our ability to control each independently from one another. Mode C was not investigated within the time period of the project.

The frame assembly and insulated reactors are shown installed in the system platform in Figure 12 (next page).

Steam Generation: The steam generation subsystem is driven by a Cole-Parmer constant flow piston water pump. An array of 7 kW of nozzle heaters wrapped around

stainless steel tubing act as the pre-heater to bring the high pressure (26 MPa) water to 350°C. This stream of subcritical steam is fed into the synthesis reactor in order to heat it into the supercritical regime and beyond, to 650°C. An Omega flow meter, FLR1007, records the flow rate and also acts as a safety mechanism, turning off the heaters if the pump has stopped operating.

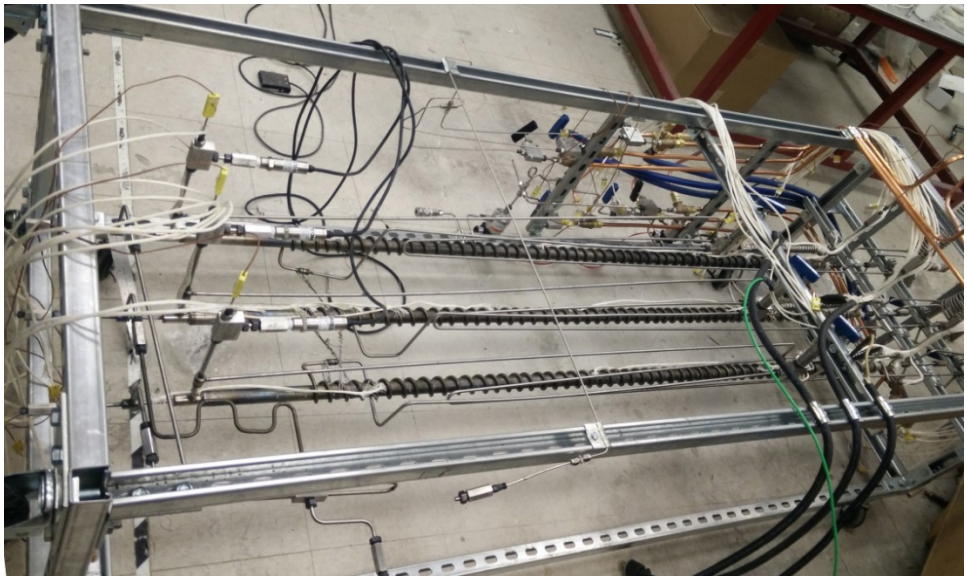

Figure 11: Synthesis reactors with Inconel 625 spiral tubing for autothermal operation, mounted on mobile frame without insulation.

Figure 12: Synthesis reactors (right) and dissociation reactors (left) standing upright and installed in the closed loop testing platform.

Experimental Results

Maximum Steam Heating (Mode A): We have successfully achieved thermal power output of over 5 kW_t. Electric preheaters were used to raise the inlet gas temperature to ~600°C. Outer wall temperatures (OR, representing gas temperature) and inner wall temperatures (IR, representing steam temperature) for the three synthesis reactors were measured, see Figure 13. Steam temperatures averaged over the three reactors are labeled at key locations in the figure. The average steam inlet temperature was lower than the desired 350°C because of an unexpected limitation to the system. The steam generator was made of stainless steel and designed with an upper temperature limit for safety of around 380°C. The steam temperature dropped between leaving the steam generator and entering the heat recovery reactor due to losses. Since the steam inlet temperature was only 335ºC, we heated the steam through the desired 300°C temperature increase to an outlet temperature of 636°C. This temperature difference, with the steam mass flow rate of 2.5 g/s, corresponds to 5.2 kW_t. It is interesting to note that the maximum steam temperature was 643°C averaged over the three reactors. The steam temperatures declined after passing the peak gas temperature; as explained previously, a better design would be to use an adiabatic reactor to allow the gas to reach its peak temperature before it enters the heat recovery reactor.

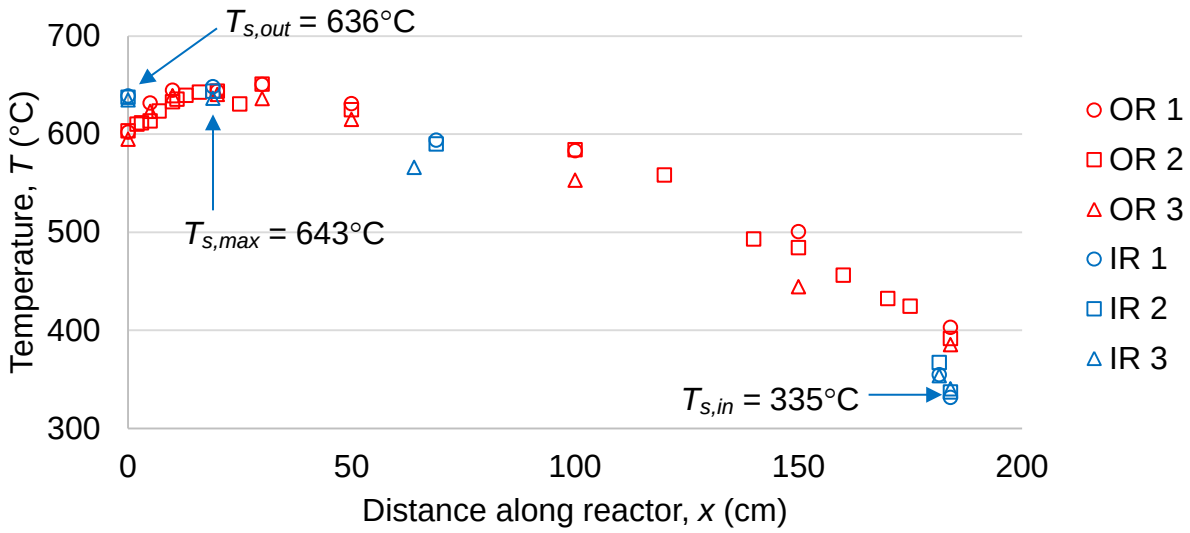

Figure 13: Temperature profiles for three reactors with 5 kW_t power output. Conditions are: $\dot{m}_g$ = 4.7 g/s, $\dot{m}_s$ = 2.5 g/s.

Autothermal Operation (Mode B): The three reactors were run in autothermal mode, with flow through the spiral tubes. Outer wall temperatures (OR), steam temperatures (IR), and spiral temperatures (SP) were measured and are shown in Figure 14. Synthesis gas enters the spirals at x = 180 cm (green symbols) having been preheated to 411°C in the recuperating heat exchanger. (Stated temperature values are averages over the three reactors.) The gas flows to the left in Figure 14, exiting the spirals at x = 0 cm at around 529°C. It is then mixed with additional cooler synthesis gas coming from the recuperating heat exchanger (discussed further below), and that mixture enters the catalyst bed (red symbols) at x = 0 cm. Its temperature at that point is around 476°C. Because it is far from equilibrium, it undergoes a large temperature increase to 610°C

(this is the outer wall temperature – the gas temperature would be somewhat hotter). Steam enters at x = 180 cm (blue symbols) at around 324°C and rises to a peak temperature of around 613°C (undergoing a temperature rise of 289°C, a little shy of the desired 300°C). It then drops significantly to an outlet temperature around 513°C, once again pointing out the value of an adiabatic reactor preceding the synthesis reactor. The power added to the steam is 845 W_t based on the inlet and outlet steam temperatures averaged over the three reactors.

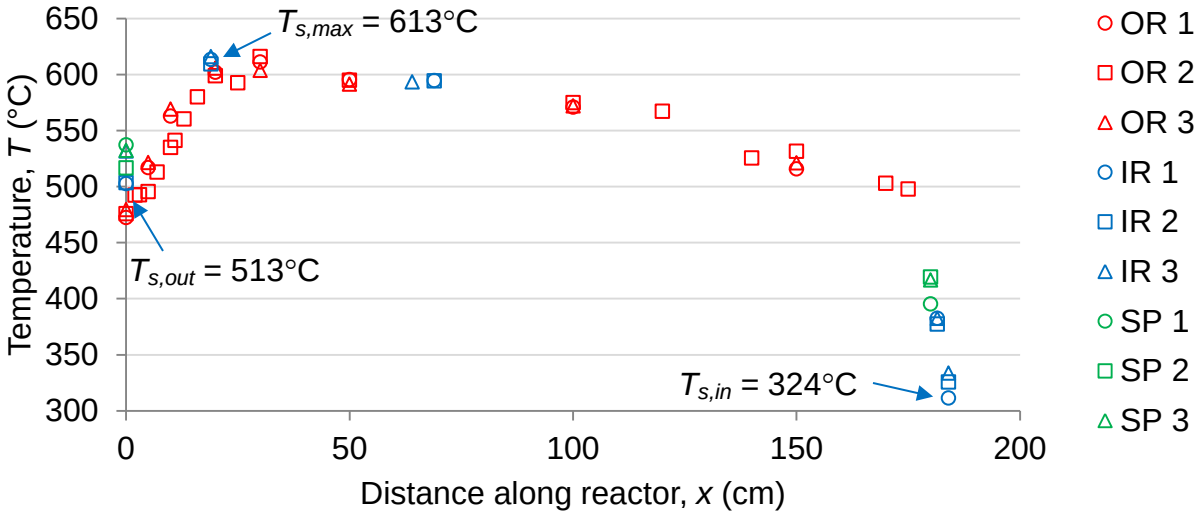

Figure 14: Temperature profiles for three reactors running autothermally, in Mode B. Conditions are: $\dot{m}_g$ = 3.3 g/s, $\dot{m}_s$ = 0.49 g/s.

As seen in Figure 10(b), in Mode B there are two streams of gas entering the catalyst bed (at the top of the reactor). One “cool” stream enters downward in the figure, coming directly from the recuperating heat exchanger and flowing through the electric heater (which was off in the current experiment). The other stream has been preheated in the spiral before entering the catalyst bed. For various reasons, the system was designed so that the "cool” stream could not be shut off entirely. It was believed that when the spiral flow valve was fully open, the cool stream flow would be relatively small, however that did not appear to be the case in practice: the spiral exit temperature was 529°C, but the temperature of the mixture entering the catalyst bed was only 476°C. We believe this is the main reason why the steam temperature didn’t rise to 650°C and this also contributed to limiting the power delivered to the steam.

Commentary: The power level of the reactor exceeded the planned capacity of 5 kW_t, but we believe that it can perform better. The maximum power capacity of the reactor is limited by the synthesis gas mass flow rate. The maximum gas flow rate achieved was 5 g/s. We believe that with slight modifications to the storage and separation subsystems, greater flow rates—and thus higher power performance—can be achieved with the current platform operating in any of the three modes. In addition, a mechanism for limiting the “cool” flow entering the catalyst bed would enable higher temperatures and power in autothermal Mode B. Finally, if the steam generator were re-fabricated of higher temperature tubing, the steam inlet temperature could reach 350°C and the synthesis reactor could heat steam from 350 to 650°C rather than from 335 to 635°C.

Catalyst Lifetime Experiments

In the ammonia industry, synthesis is typically carried out at temperatures below around 550°C, thus iron-based catalysts are not used at higher temperatures. We believe the best choice for the high-temperature catalyst is an iron-cobalt material that can be used at temperatures up to 700°C, has activity that is almost as effective as an iron-based catalyst, and was successfully used at 700°C and above at ANU [23]. However, we have not been able to find a current supplier for this catalyst. Presumably if there were a market for it, it could be produced again.

In the absence of an iron-cobalt catalyst, we operated our reactors with iron-based catalyst. Thus, one task was to conduct catalyst lifetime testing to determine if there was any observed degradation in catalyst performance over the duration of the project. This was accomplished in part by observing the behavior of the intermediate scale reactor over the course of 167 hours of intermittent operation at high temperatures. We compared two outputs: (a) the rate of temperature rise near the bed inlet, which reflects the reaction rate there, and (b) the ammonia yield.

Concerning the rate of temperature rise, Figure 15 shows the outer wall temperature for six experimental runs (without steam) with nominally the same conditions of $\dot{m}_g$ = 1 g/s and $T_{g,in}$ = 520°C. There is some variation in the initial rate of temperature rise, with seemingly some increase between January and March, and then the two August runs having the lowest initial rate of temperature rise. There is also a fair amount of variability – for example, it can be observed that beyond the peak temperature there is a spread of about 10°C, with one of the August runs near the top of the range and the other near the bottom. There are a variety of factors that could cause variability. We are aware, for example, that we did not have good control over the ammonia mass fraction in the inlet stream (see next paragraph), and this can have a strong effect on the reaction behavior. The results are inconclusive, but some sort of degradation in the iron-based catalyst behavior cannot be ruled out.

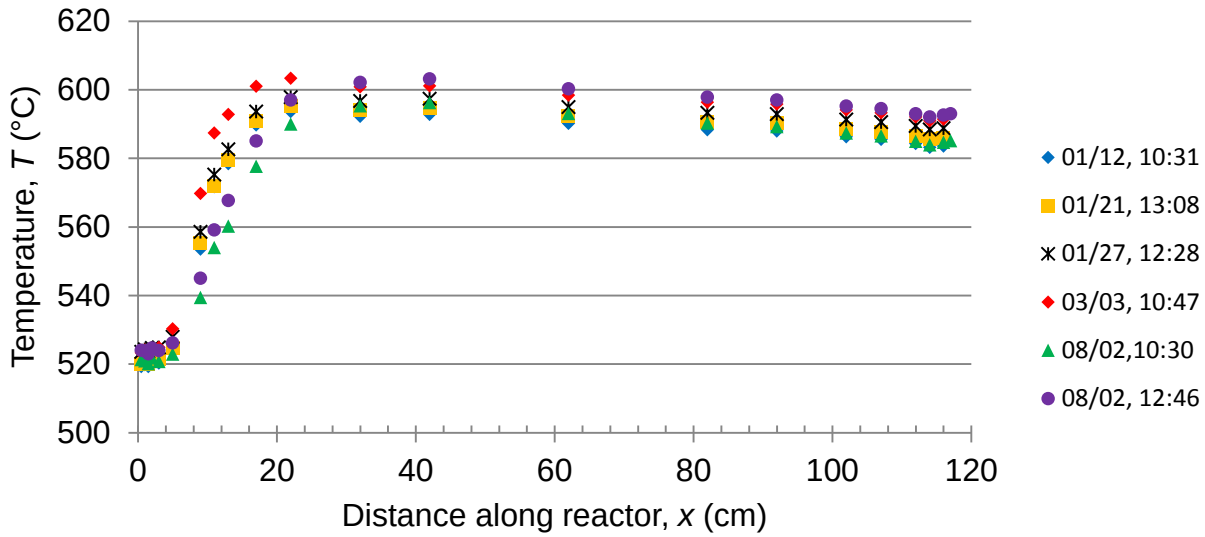

Figure 15: Comparison of reactor temperature rise over time.

Ammonia inlet and outlet mass fractions are shown in Table 1 for the same six experimental runs as in Figure 15. Although we are not confident of our absolute composition measurements, we believe based on other evidence that there is an offset rather than a random error. It appears therefore, that if anything, the yield is higher on the later dates, suggesting that any possible change in catalyst activity over time has not resulted in a dramatic impact throughout the reactor.

Table 1: Ammonia Yield over Time

Date, Time	Inlet NH3 fraction	Outlet NH3 fraction
01/12, 10:31	0.061	0.176
01/21, 13:08	0.062	0.171
01/27, 12:28	0.059	0.173
03/03, 10:47	0.046	0.176
08/02, 10:30	0.045	0.191
08/02, 12:46	0.045	0.184

Another element of the experimental protocol was to characterize the catalyst before and after reactor testing, to observe any changes that may have occurred, such as physical changes or poisoning. Scanning electron microscopy (SEM) was used to obtain images and particle sizes, while energy dispersive spectroscopy (EDS) was used to identify the composition of the catalyst.

The before tests were conducted on the iron oxide catalyst after grinding and sieving to size (0.4 to 0.6 mm). After the reactor was run for a total of 167 hours, it was cut open and catalyst was removed. Catalyst samples were extracted at three different locations: 0 cm, 18 cm, and 120 cm from the start of the bed. Note that the before particles were not reduced, but the after particles were, so they would not be expected to be identical in appearance.

Figure 16 shows SEM images with the same magnification (X35) that compare the particles from before and after the reactor testing. As shown in Figure 16(b), the particle sizes after testing at 0 cm are significantly smaller compared to the particle sizes from before the reactor testing (Figure 16(a)). At 18 cm and 120 cm, the particle sizes remain comparable to the before images, as shown in Figure 16(c) and (d).

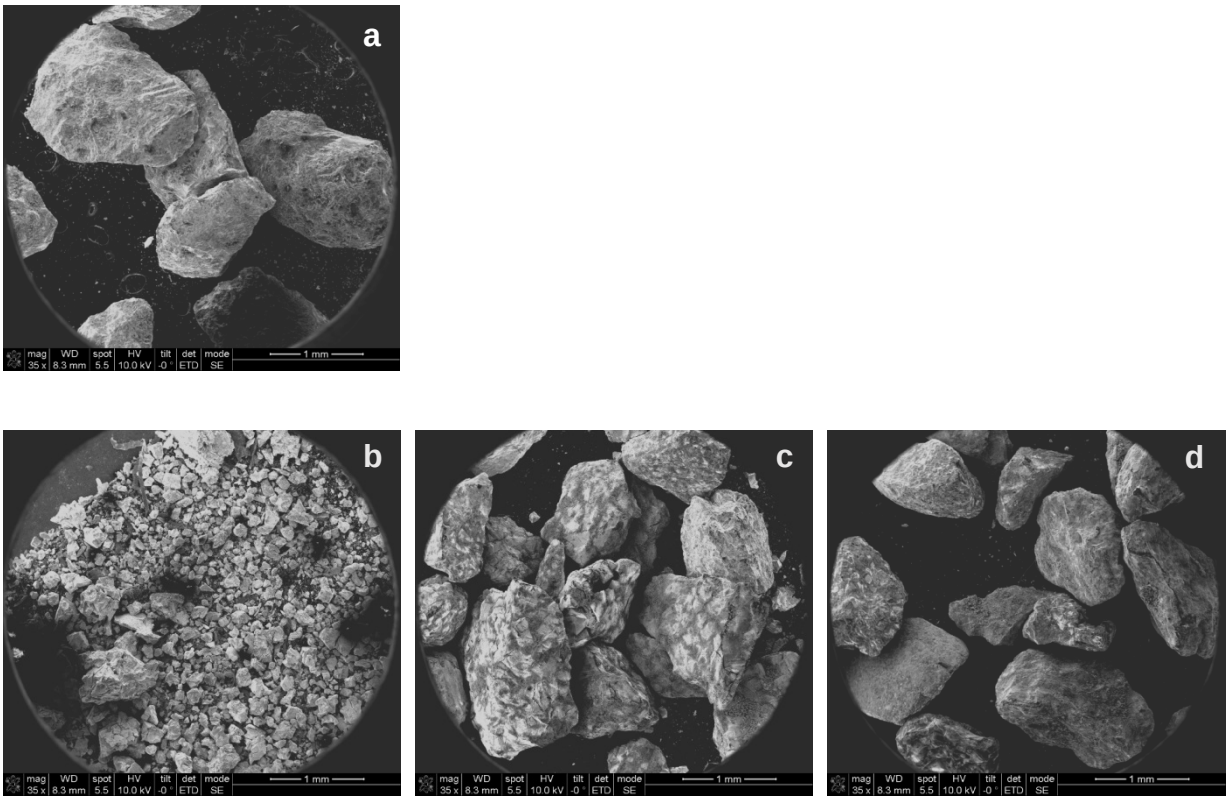

Figure 16: SEM images of the iron catalyst with magnification of X35, (a) before testing, and (b)-(d) after reactor testing at locations (b) 0 cm, (c) 18 cm, and (d) 120 cm.

Further SEM images were taken of the sample obtained at 0 cm. Figure 17 shows an image of the particles with a magnification of X1972. The particle sizes are on the order of tens of micrometers. EDS analysis performed on both particles in Figure 17 showed that the particle marked with an “o” is in fact traces from the reactor wall, presumably introduced when the reactor was cut open. The particle marked with an “x” is iron catalyst; it displays a porous surface as would be expected after reduction.

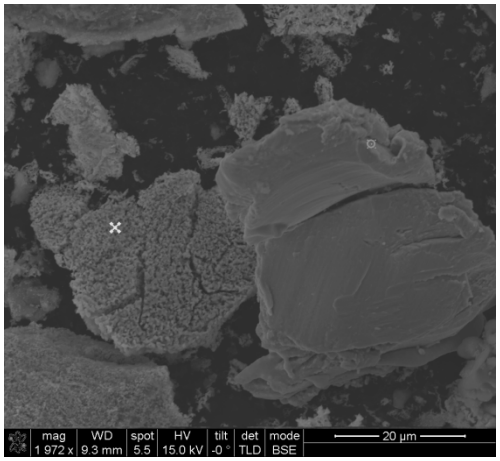

Figure 17: SEM image of the catalyst sample obtained at 0 cm from the start of the bed after reactor testing with magnification of X1972.

Unfortunately, we cannot definitively determine the cause of the smaller sized particles near the bed inlet. Possibilities include: (a) The container that held the ground particles before loading could have settled with smaller particles at the bottom, which then ended up at the top (inlet) of the reactor when loaded. (b) After loading, smaller particles settled to the bottom of the reactor and fell through the mesh that was used to hold the catalyst in place. They were then carried around the loop and redeposited at the bed inlet. (c) Catalyst particles cracked in situ due to thermal stresses that could have been highest near the bed inlet.

The compositions of the catalyst samples before and after reactor testing were determined using EDS analysis. For the before samples, iron and oxygen are the predominant species (58% Fe, 33% O by weight), and carbon is present at ~3%. Small traces of Al, Si, K, and Ca were also identified; all of these except for Si are consistent with the known inorganic promoters in the catalyst. An elemental map was generated to show that the carbon identified was not contamination on the catalyst, but the carbon tape used to load the catalyst particles. After reactor testing, the samples at 0 cm were ~80% Fe and less than 5% O (consistent with having been reduced), around 3% C, and traces of the other mentioned elements. Further downstream the Fe weight percent decreased and the O and C weight percents increased. At 1.2 m, a typical sample was 70% Fe, ~6% O, and ~12% C. It is possible that iron carbide is forming from the unintended presence of hydrocarbons, and that this occurs preferentially toward the exit as hydrogen content in the gas stream drops. This is only speculation at this time.

In summary, the catalyst lifetime testing has shown some anomalies, but a more controlled testing protocol would be required to fully understand their causes. If iron-based catalyst is unsuitable at the elevated system temperatures, another catalyst such as iron-cobalt should be used.

Underground Storage (Task 3.1)

Options for Underground Storage

A key aspect of the ammonia based TCES system is the storage of the hydrogen and nitrogen gas mixture that embodies the stored energy. Pressurized above-ground storage options have been considered previously and are too expensive to meet the Sunshot cost target. As part of this project, cost effective underground solutions were sought. A key motivation in pursuing underground solutions is that the earth itself will offer the pressure containment and so result in a low cost solution.

A review was conducted of existing and potential approaches to high-volume, high-pressure, underground gas storage. Relevant existing practices include seasonal and peak natural gas demand “smoothing” and hydrogen containment. The majority of the literature relates to the former as this practice is widespread in the well-established fossil fuel industry. The technical and economic potential of other options which have not yet been deployed commercially for gas storage was also explored, including well-drilling and tunneling.

All underground storage approaches are significantly influenced by geological factors. Rock types and local stress conditions will have significant effects on cost of construction, permeability, pressure containment, and self-supporting capability. For

solar energy storage, within the constraints of high DNI, sites would presumably be chosen to allow for least-cost underground storage.

For the various underground storage approaches, there is a minimum amount / pressure of the stored gas that must be left in situ--so-called “cushion gas”—in order to preserve the integrity of the underground store. The storage system will cycle in pressure between maximum and minimum values. If the synthesis reaction is operated at a fixed design pressure (or between narrower limits), then feed gas will need to be compressed for much of the time. Gas storage should be designed for an economically optimal storage pressure independent of the reaction system. A 220 MW_t plant with 6 hours of storage would require 1320 MWh of storage corresponding to a volume of ~12,000 or 18,000 m^3 for storage pressures of 30 MPa or 20 MPa (with an enthalpy of reaction of 66.8 kJ/mol NH_3). For the purpose of making conservative initial estimates, the lower pressure value and 33% cushion gas was assumed, for a total of ~24,000 m^3 of storage.

The storage of the gases and the resultant energy storage density are completely independent of the degree of reaction achieved in either the exothermic or endothermic reactors for the ammonia system, due to the feature of phase separation. Considering the energy recovery side, hydrogen and nitrogen gases are continually drawn from storage and reacted; the partially converted products are returned to storage where they separate via condensation of the ammonia and can be reused until essentially the entire inventory of hydrogen/nitrogen gas mix (less any cushion gas) has been converted to ammonia.

Numerous alternatives for storage of gas mixtures were researched with reference to an extensive literature (e.g., [24-33]), namely salt caverns, rock caverns, aquifers, depleted oil/gas wells, large diameter drilled shafts, micro tunnel boring, large diameter tunnel boring, steel pressure vessels, gas pipelines, and reinforced concrete pressure vessels. The alternatives were all scored on attributes such as cost, site constraint, leakage potential, safety, etc., according to the Analytic Hierarchy Process [34]. The two highest ranked options, salt caverns and shaft drilling, have been pursued further and both are concluded to be viable. These two are now discussed in further detail.

Salt caverns

Salt caverns can be mined in either salt domes or salt beds. Mining of salt caverns is a simple process achieved via solution mining, or leaching, whereby freshwater is pumped into the salt dome and brine is extracted. Over 2000 salt caverns are in operation in North America for hydrocarbon storage, including ~500 in Texas alone [29]. The use of caverns for gas storage is well established, with 31 such systems operating in the USA in 2008 [30]. Caverns are typically at depths between 200 to 2,000 m and can be up to 500,000 m^3 in volume, capable of tolerating pressures of up to ~50 MPa [31].

Consideration of the potential for gas contamination is required with methane, nitrogen, carbon dioxide, and hydrogen sulfide commonly occurring in salt deposits. The rock salt itself, however, is chemically inert to hydrogen and is one of the only rock formations with permeability low enough to contain hydrogen gas.

Pure hydrogen or hydrogen-rich gas mixtures have been stored in salt caverns at the following sites:

- Yorkshire, UK: for many years British chemical manufacturer ICI stored around 2000 m^3 (1 million Nm^3) of 95% H_2 and 3-4% CO_2 at 50 MPa in three salt caverns at 400 m depth [31].
- Kiel, Germany: a 62% H_2 town gas mixture was stored in a 32,000 m^3 salt cavern at 8-10 MPa [24].
- Texas, USA: Praxair currently operates a 470,000 m^3 (71 million Nm^3) hydrogen storage plant at 15 MPa, with 44% cushion gas by volume.

A Department of Energy report from 2008 into the economic feasibility of syngas storage, reproducing Taylor et al. [32], suggests \$43-53/m^3 when escalated to 2014. For a 24,000 m^3 volume, a very low thermal storage cost of \$0.80–0.95 per kWh results. Consultation with a license holder of an as yet undeveloped salt deposit suggests current values are in the range of \$1- \$2 per kWh [33]. Though the costs quoted here involved mining of caverns much larger than 24,000 m^3, costs are low enough to suggest economic feasibility for salt cavern storage.

Use of solution mined caverns in beds or domes of rock salt proves to be an established technology for the storage of gases including hydrogen, at the high pressures needed for the ammonia system. Most importantly the direct cost contribution of establishing such a cavern is only approximately \$1/kWh_t. Typical caverns can be 10 or more times larger than required for the 100 MW_e, 6 hours of storage terms of reference for ELEMENTS. It is apparent however that with size not being a limiting factor, this is a solution that may be even better suited to offering 15 hours or more of storage for baseline configured plants, and/or for extending the system to power blocks of 500 MW_e or so, which are actually preferred for existing supercritical steam power blocks.

The need to maintain a minimum buffer pressure in salt caverns, together with the cost effectiveness of very large volumes, also has the benefit that a system can be configured such that the storage system operates within a window of varying high pressure that is suitable for operation of the ammonia synthesis reactor. In this way the need for complex and expensive gas compression can be much reduced.

Suitable salt deposits are present on every continent including North America and there is a good coincidence with high DNI areas (see Figure 18).

The availability of salt deposits is certainly sufficient for ammonia-based CSP systems to be technically capable of providing large fractions of global electricity needs. Despite this, it must be acknowledged that siting for suitable salt deposits is a significant constraint. This motivates continued investigation of other more universally applicable approaches.

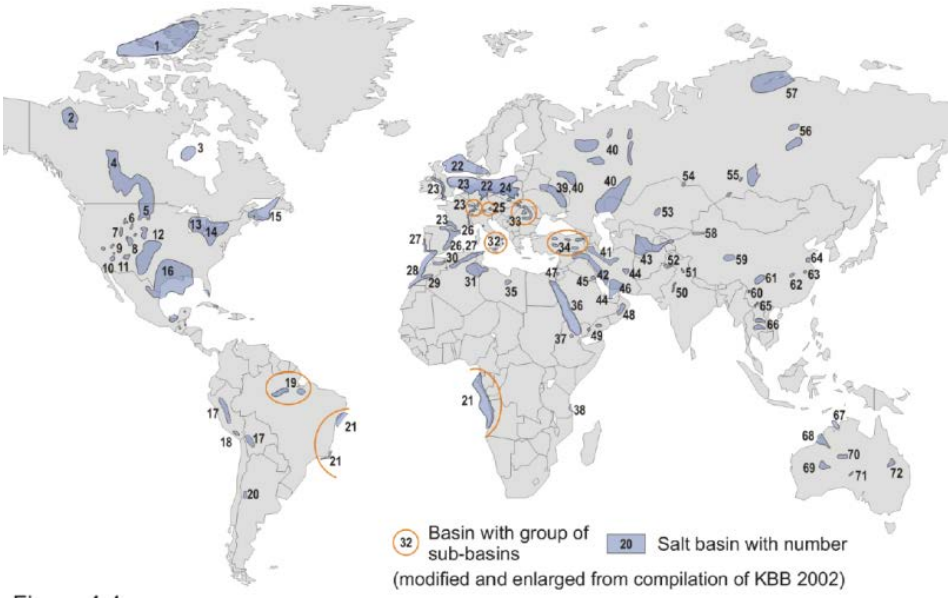

Figure 18: Location of salt deposits globally (from Solution Mining Research Institute).

Shaft drilling

The second approach which is under continued investigation is large diameter shaft or bore drilling. This is also an established technology although not directly applied to gas storage previously. Shaft drilling is routinely carried out at up to 7.5 m diameter and to depths of 1000 m. The concept is to use shaft drilling to create a gas pressure store. This solution appears to also be suitable for near term commercial application.

The team has consulted with Shaft Drillers International (SDI) LLC (http://www.shaftdrillers.com/), one of the global leaders in the field of shaft drilling. SDI reports that excavation of a "series production" shaft with their new machine concept would cost around $400.00 per cubic meter.

It is clearly a major project in its own right to progress this idea to a workable gas storage solution. Nonetheless, $400/m^3 translates to an energy storage specific cost of $4.83/kWh$_t$ if no buffer gas is required, rising to $7.20/kWh$_t$ if 33% buffer is allowed. Given that such a system would be fabricated at atmospheric pressure, operation without buffer allowance is plausible. These storage costs are sufficiently below the SunShot $15/kWh$_t$ target to conclude that this is also a potentially viable approach.

Commentary

At the end of the project there are two particularly promising underground storage approaches for storing the hydrogen and nitrogen gas mixtures: solution mined salt caverns and large diameter shaft boring. Both are much more widely applied technologies than is usually realized. Salt caverns offer storage costs that could be as low as $1/kWh$_t$, but although suitable salt deposits are quite common they are not universally available. Shaft drilling offers a more expensive but more universally applicable solution that should still be within the cost target. Together these two options answer the technical challenge associated with storage of gas phase components.

Endothermic Reactor/Receiver (Task 4.1)

Receiver concept for tower plus heliostat field

It is important to demonstrate that the full system, including integration of the endothermic reactors, is plausibly both technically and economically feasible.

The long history of work at ANU upon which this initiative builds included demonstration of the operation of a high temperature ammonia dissociation receiver on a 20 m^2 dish concentrator [11]. The receiver concept comprised a series of reactor tubes in a conical arrangement within a cavity receiver. This worked well. Of particular importance was the finding that multiple tubes connected in parallel flow via a simple manifold were able to all work within a reasonable range of a desired operating temperature. This was achieved by adjusting their pressure drop characteristics at ambient temperature during manufacture. It is an important finding that this was a workable solution and that active flow control was not required for each tube. Based on this success with a prototype receiver, it can be claimed with reasonable confidence that the concept could be adapted to any size of dish. Dishes are however the least commercially mature CSP technology.

The most likely concentrator system candidate for applying the ammonia system in the near-term is a tower based system. The SunShot ELEMENTS program calls for tower system designs of 100 MW_e and 6 hours of storage. Designing a receiver for a tower system is a major project in itself. The goal for this task was to establish unequivocally that developing such a design would be possible.

Design Issues: The assumption was made that packed bed catalytic dissociation reactors would continue to be used for a tower receiver and that high system pressures that are dictated by the kinetics and exergy requirements of the exothermic heat recovery process would be required; the designs discussed below are all for a 30 MPa system pressure. As well as containing the pressure, the receiver reactor design must be able to convert sufficient ammonia to meet the thermal power requirement and do so at reasonable operating temperature. In developing a concept, there are three key issues driving design:

- The pressure drop along the packed bed, which should be kept reasonably small.
- The limitations of heat transfer from the reactor wall to the innermost catalyst particles.
- The total volume and hence materials cost of the reactor wall material and catalyst material.

The combination of pressure containment requirements and heat transfer limitations essentially mandates tubular packed beds. Diameter and length plus operating temperature become the key variables. There is the possibility of considering tubular passages within a metal absorber sheet, integral tube sheets, or individual tubes mounted in some arrangement. Individual tubes have some key inherent advantages. As small modular units they are very suitable for mass production in an automated factory environment. Individual tubes coupled to manifolds with smaller bore tubing and then mounted in suitable frames are inherently flexible and free of potential thermal

stresses that large solid structures can experience. They are easier to replace for maintenance purposes if needed.

Tube reactor modules: To model a receiver reactor system thoroughly requires simultaneous and iterative solution of:

- The incident flux distribution on a receiver
- The effects of partial reflection of radiation
- The chemical conversion process driven by the net input of energy to the reactor tube
- Thermal convection, radiation, and conduction losses that depend on temperature that is in turn determined by the reaction process.

For the purposes of conceptual design, the process can be progressed by:

- assuming a desired temperature distribution on an individual tube (isothermal in the first instance) and determining the resulting performance and absorbed energy profile,
- estimating a geometric arrangement likely to deliver the desired net absorbed flux profile, and
- estimating receiver efficiency from the required size and operating temperature.

Tube reactors with varying diameter, length, flow rate, and operating temperature have been modeled. For this investigation, the same iron-cobalt catalyst (DNK-2R) used successfully in the ANU dish prototype has been assumed.

An investigation of the effect of increasing the tube size was carried out. The ANU tube design (which was designed for 30 MPa and 700°C operation) was taken as the baseline, and was increased in length and diameter with wall thickness-to-diameter ratio kept constant. For each geometry, the flow rate was adjusted until the total exit dissociation was ~70%.

Smaller tubes were found to absorb heat more effectively per unit volume. In this case, heat transfer from the outer wall more effectively raises the average temperature of the bed, increasing the average reaction rate and thus decreasing the total tube volume required. In practice, smaller tubes will be more difficult to manufacture and pumping losses due to pressure drop through the bed will be larger. It was judged that a 5 cm diameter bed system should be used as a first estimate. The 5 cm diameter tube model has a length of 2.7 m and achieved 70% dissociation at a flow rate of 8.5 g/s.

Increasing the temperature of the outer wall can be seen to increase the thermal capacity of a tube owing to the higher average reaction rates achieved. The impact of increasing this temperature to 625°C, 650°C, 675°C, and 700°C was investigated, with the results depicted in Figure 20.

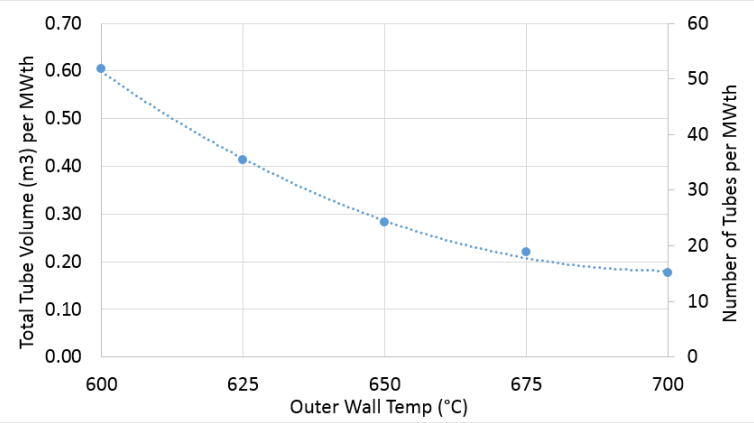

Figure 20: Total tube number and volume per MW_t of absorption vs. isothermal outer wall temperature (70% dissociation, 5 cm catalyst bed outer diameter and 2.7 m tube length).

In practical operation a reactor tube's behavior is determined by the level of incident solar flux on it. This can be adjusted via the design of the receiver geometry. Temperatures will also start lower at the point of ammonia feed and rise towards the exit of the bed. A preferred receiver design will be one where the higher temperature ends are positioned further from exposure to thermal losses to ambient conditions by shielding them behind the lower temperature parts. Investigation of the relative performance of reactor tubes of varying cold end temperature for a maximum 700°C catalyst bed exit temperature is shown in Figure 21.

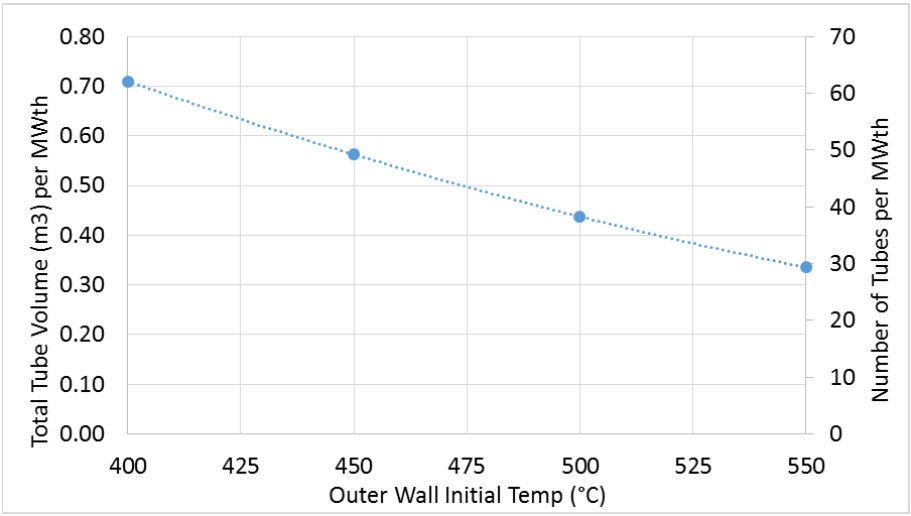

Figure 21: Total tube number and volume per MW_t of absorption vs. inlet end outer wall temp (70% dissociation, 5 cm catalyst bed outer diameter reactor length 2.7 m, outer wall temp rising to 700°C).

Increasing the inlet end outer wall temperature ensures higher average bed temperatures, and hence higher reaction rates and greater heat absorption per unit of tube volume. These results allowed a technically feasible receiver design to be developed that aimed to minimize the temperature of exposed surfaces while achieving the desired energy collection within the space available.

Tower receiver concepts: Tower heliostat fields come in two basic configurations. A field of heliostats completely surrounding the central tower can be applied to a cylindrical receiver that is irradiated from every direction. Alternatively, a cavity receiver will have a finite acceptance angle and the field of heliostats will be limited to an approximately elliptical area in the direction of the cavity's view and with an extent dictated by its field of view. Cavity receivers offer lower thermal losses than surround field cylindrical receivers for a given operating temperature. On the other hand a surround field arrangement makes more cost effective use of the investment in tower and receiver and balance of system.

SAM 100 MW_e salt tower as baseline. The NREL System Advisor Model has a molten salt power tower model for a 100 MW_e, 10 hour storage plant with the characteristics shown in Table 2. This is understood to be similar to the Crescent Dunes plant in Nevada. The approach taken here is to develop a conceptual design for an ammonia dissociation receiver that fits within the same cylindrical size envelope as the molten salt receiver currently used.

Table 2: Characteristics of SAM tower receiver

HTF inlet temperature	290°C
HTF exit temperature	574°C
Diameter	17.67 m
Height	20.41 m
Thermal capacity	669.9 MW_t
Emittance	0.88

A proprietary design of a receiver of the same thermal capacity as the SAM case has been completed. Generally speaking, the design consists of tubes arranged to create a "petticoat" receiver of similar size, as illustrated in Figure 22(a).

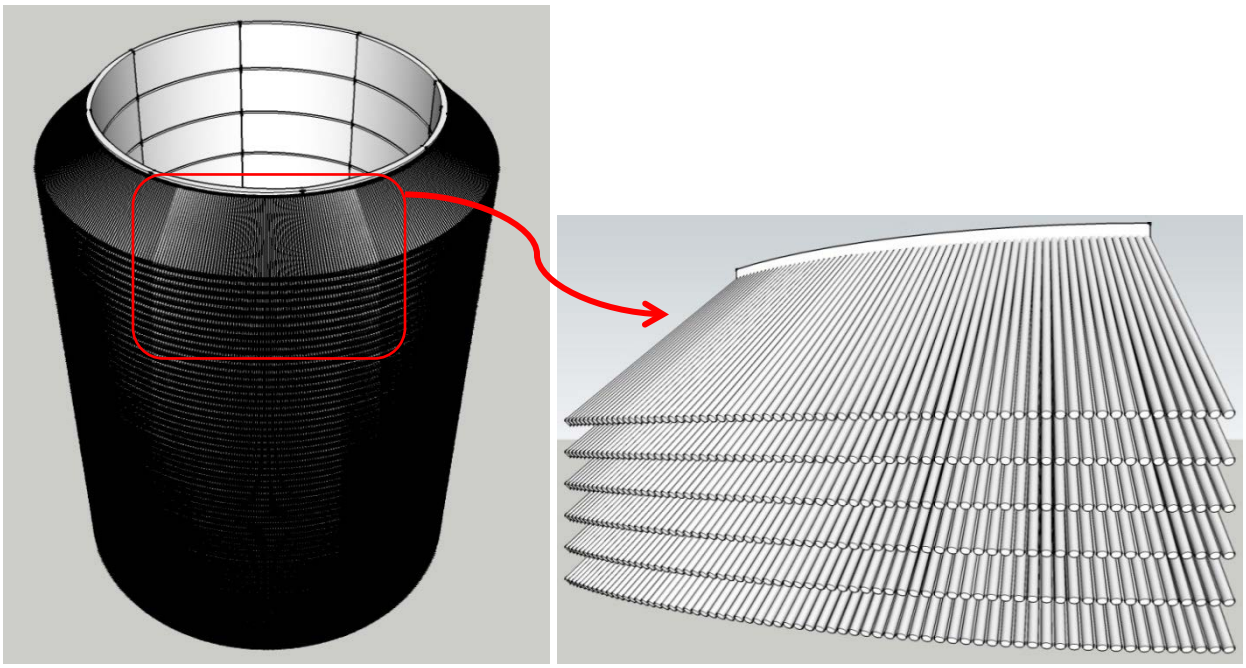

(a) (b)

Figure 22: Concept sketch of (a) entire receiver and (b) close view of one of 80 individual panels.

Estimating thermal efficiency

The SAM molten salt receiver has essentially flat panels that house passages for the salt fluid as it is heated from an inlet temperature of 290°C to 574°C. Overall the average surface temperature is 432°C. An 89% receiver efficiency is achieved at midday peak solar input conditions. The reactor tubes contemplated for the ammonia dissociation receiver operate at higher temperatures overall however to counter that there are some geometrical advantages that can be leveraged. The tubes would be arranged such that the lower temperature inlet conditions at around 450°C would be outermost and the higher temperatures towards the inside.

The key concept however is the petticoat arrangement of the reactor tubes in a series of tight packed skirts around the receiver. With the downward angle of the tubes, the gaps between adjacent rings will behave like a cavity. The overall radiation and reflection losses will be reduced. A stagnant, stably stratified air space will also form inside, with convection losses considerably reduced over those of a flat panel receiver of the same temperature.

Thermal loss calculations for SAM molten salt receiver: In order to calculate the thermal efficiency of our receiver design, we developed a UCLA thermal loss model based on the methodology used within SAM. We tuned and validated the UCLA model by replicating the results for the SAM molten salt receiver. The conditions of the power plant and molten salt receiver modeled in SAM are given in Table 3.

Thermal loss calculations for ammonia dissociation receiver: The UCLA thermal model has been used to calculate the radiation and convection losses from the ammonia dissociation receiver. The radiation losses were estimated using a simplified

geometry that assumes the “petticoat” is assembled on a flat base and each skirt is horizontal. We have used the *outer* circumference of the receiver as the width, *W*, of the skirts, which overestimates radiation losses. For calculating convection losses, the air in the cavities is assumed to be stagnant. This creates a continuous outer receiver “surface” consisting of the skirt tips and gap ends, which is assumed to be at the tip temperature. The total convection losses were calculated using the mixed convection correlation in SAM [35].

Table 3. Conditions of plant and molten salt receiver modeled in SAM

Design Power	**100 MW_e**
Storage duration	10 hours
Thermal capacity (energy absorbed)	669.9 MW_t
HTF inlet temperature	290°C
HTF exit temperature	574°C
Receiver Diameter	17.67 m
Receiver Height	20.41 m
Wind speed	7 m/s
Dew point temperature	-8°C
Ambient Temperature	27°C
Receiver Emittance	0.88

The ammonia dissociation receiver was modeled for the design conditions of T_{base} = 700°C, T_t = 450°C, corresponding to a thermal capacity of 669.9 MW_t. The thermal losses and thermal efficiency for the SAM molten salt receiver and the dissociation receiver are compared in Table 4.

Table 4. Comparison of losses for molten salt receiver and ammonia dissociation receiver

	Molten Salt	**Ammonia Dissociation**
Thermal capacity (energy absorbed)	669.9 MW_t	669.9MW_t
Radiation losses	19.4 MW_t	23.8 MW_t
Convection losses	15.5 MW_t	14.6 MW_t
Efficiency	94.8%	94.6%

The radiation losses are higher for the dissociation receiver, which is to be expected because of its higher temperature range. On the other hand, the effect is perhaps not as extreme as might be anticipated because of the effective shielding of the highest temperatures deep within the cavities formed by the tubes. The convection losses are actually predicted to be lower for the dissociation receiver. This unanticipated result can be readily explained. For both receivers, convection is modeled from the same area – the outer perimeter of the receiver. For the dissociation receiver, that area is assumed to have a uniform temperature of 450°C. For the molten salt receiver, even though the *average* temperature is slightly lower (432°C), the temperature varies from 290°C to 574°C along the height of the receiver. Natural convection has a nonlinear dependence on temperature, with higher temperature regions of the receiver having higher heat transfer coefficients, leading to higher overall convection losses for the molten salt receiver.

Comparing the efficiency of the ammonia dissociation receiver (94.6%) to the efficiency of the molten salt receiver (94.8%), the design of the ammonia dissociation receiver is extremely promising.

Commentary

A conceptual design of an ammonia dissociation receiver/reactor has been developed. This receiver fits into the same size cylindrical envelope as the molten salt receiver in SAM, and has the same design thermal capacity. In the current quarter, we have established that the thermal efficiency of this receiver exceeds 90% and is very close to the thermal efficiency of the SAM molten salt receiver. Thus, this investigation has established unequivocally that a surround field tower system based on ammonia dissociation reactor tubes is technically feasible.

Optimization (Task 6.1)

An important task was to design an optimized, full-scale synthesis system for a 220 MW_t plant with 6 hours of storage. The synthesis system includes the heat recovery reactor and preconditioning system (described in detail shortly), all of which must be simultaneously optimized. Thus, a multi-parameter optimization algorithm was needed.

Multi-parameter Optimization Algorithm

The design optimization problem for an objective function $f(x)$ that depends on multiple design variables $x = (x_1,x_2,\ldots,x_n)$ can be written as:

$$\text{Minimize } f(x)$$

$$\text{Subject to the constraints:}$$
$$G_j(x) \le 0, \quad j = 1,m \tag{8}$$

$$\text{Over the domain:}$$
$$x_L \le x \le x_U$$

where x_L, x_U are lower and upper bounds for the design variables. We chose to use a multistart algorithm to solve the optimization problem, in order to maximize the probability of finding the global minimum. Multistart methods generate random initial design points in the feasible design space and perform local searches from them. These methods are stochastic in the sense that convergence is asymptotic. That is, roughly speaking, the probability of converging to the global minimum increases with the number of sample starting points. In this work we used a Bayesian approach in order to minimize the number of local searches. For this purpose the sampling distribution is changed based on the results of the previous local minima found. This is done in order not to explore regions in which the probability of finding a new minimum is low. The sampling process stops when the current objective function is lower than the expected objective function if a new local search were performed. Note that the distribution is updated after each local search using Bayes Theorem (for further detail, see [36]). In simple words, the algorithm stops when the probability of finding new local minima is low. Even though multistart methods only guarantee a certain probability of finding the

global solution (which is the case for most global optimization methods) they are efficient in the sense that they minimize the number of local optimizations.

The System to be Optimized

The heart of the synthesis system is the heat recovery reactor (HRR), in which energy is recovered from synthesis and transferred into supercritical steam. The HRR is shown schematically to the far right in Figure 24. As mentioned previously, the synthesis gas entering the HRR must first be preheated in a "preconditioning system," which can include three components: a recuperating heat exchanger (RHX), an autothermal synthesis reactor (ATR), and an adiabatic reactor (ADR). In Figure 24, synthesis gas enters at the left having come from storage. It passes through the RHX, where it is preheated by the exiting gas. It then flows through a passage in an ATR, where it is further preheated. At the ATR exit, the gas flow splits. One portion (dashed green line) flows back through the catalytic bed of the ATR. The remainder (dotted green line) continues to the ADR where it reacts and its temperature increases further. Finally the preconditioned gas enters the HRR where it continues to react and heats steam.

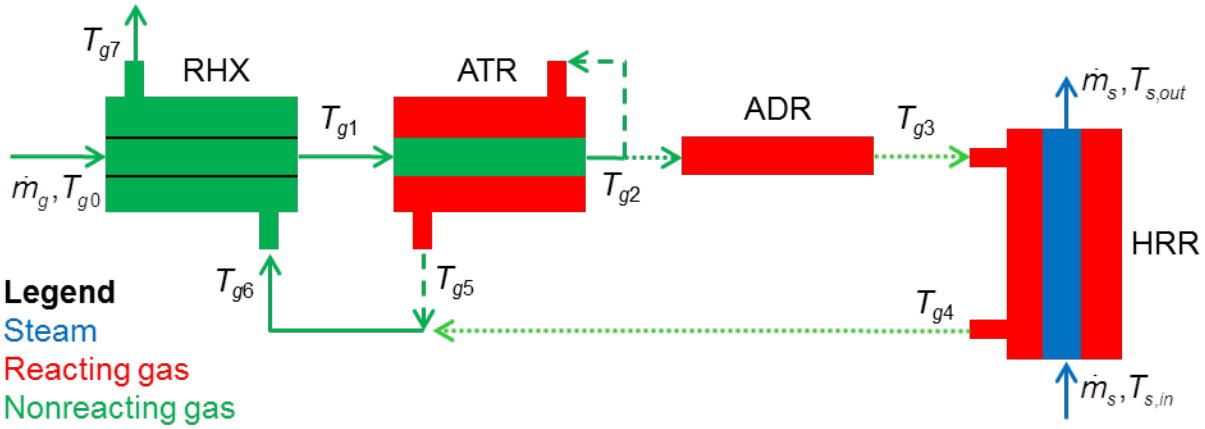

Figure 24: Schematic of the synthesis system, including the heat recovery reactor and preconditioning system.

There are trade-offs between the different components. As one example, if the heat recovery reactor were optimized in isolation, it might appear advantageous to use a very high gas mass flow rate in order to keep the HRR small. However, this could result in a large autothermal reactor in order to preheat the incoming gas. Thus the entire system must be optimized simultaneously. Note that the objective function is defined as the wall material volume of *all* components combined, per unit of thermal power delivered to the steam.

In an earlier quarterly report, we indicated that a modular design of the HRR appeared to be promising, in which different designs were used in different steam temperature ranges. In the end, when optimized as part of the entire system with preconditioning included, the benefits were more modest and did not appear worth the added complexity.

As previously noted, the HRR is modeled as a tube-in-tube configuration (Figure 2). In practice, there would be many tubes, and they could be arranged in a shell-and-tube configuration. The ATR is modeled in the same manner, except that gas flows in the inner tube instead of steam. In practice it could be advantageous to arrange the steam tubes and autothermal gas tubes all within the same catalyst-filled shell.

The recuperating heat exchanger was modeled using the Kern method [37], which provides a simple and rapid calculation of tube and shell-side heat transfer coefficients and friction factors. For a required heat transfer performance, the Kern method enables selection of the number, diameter, and length of tubes; the number of baffles; and the size of the shell. It also calculates the resulting pressure drop. We are not reporting on the details of the recuperating heat exchanger design here to save space (and because it is not a focus of our research). We will report the wall volume and heat transfer area of the RHX and include it in the cost estimates in the next section.

Returning to the tube-in-tube configuration of the HRR and ATR, the optimization procedure finds the best conditions for a single tube that minimize the wall material volume per unit power delivered to the steam; once these conditions are found, the requirement of a 220 MW_t system determines the number of tubes for the HRR and ATR. Concerning the adiabatic reactor, as mentioned earlier a certain volume of catalyst is required which can be arranged in any number of tubes of desired diameter and length. For simplicity, we chose to make the adiabatic reactor tubes an integral part of each heat recovery reactor tube, therefore the outer diameter, gas flow rate per tube, and number of tubes are the same for the ADR and the HRR.

There are eleven design variables (x in Eq. 8) that are optimized for the HRR, ATR, and ADR (and additional variables for the RHX). The HRR and ATR each require two diameters, D_2 and D_3 (with D_1 and D_4 determined by Eq. 7); two mass flow rates; and one temperature. The adiabatic reactor only requires one inlet temperature. Since the components are arranged in series with the outlet temperature of one being the inlet temperature of the next, the model can determine the required lengths of each component (or volume, in the case of the ADR) to achieve the outlet temperatures.

There are two physical constraints imposed on the system (G_j in Eq. 8).

1. The pumping power is constrained to be less than 10% of the power delivered to the steam.
2. The RHX is required to heat gas from T_{g0} to T_{g1}, utilizing exhaust gas entering at T_{g6}. Clearly, T_{g6} must be higher than T_{g1}. This is implemented as a constraint on T_{g6} expressed in terms of the effectiveness of the RHX. We imposed effectiveness ≤ 0.8.

A proprietary optimized design has been completed.

Note that although upper and lower bounds were imposed for all the design variables, in most cases the optimal solution was not at one of the bounds. The only exception was D_2 for the steam reactor, which selected the minimum value of 0.32 cm (1/8”). We imposed this bound because it is the smallest widely available commercial tube size.

In the next section, a cost estimate is performed for the proprietary design, as well as other components of the thermochemical energy storage system.

Cost Estimation (Task 6.1)

The goal of the ELEMENTS program is to reach an installed cost of thermochemical energy storage of \$15/kWh$_t$ of capacity. In this section we analyze the ammonia based system in light of the information obtained from other aspects of the project to assess the likelihood that this target can be met. The context is taken to be the comparison with a default two tank molten salt energy storage system, where the boundaries of the energy storage subsystem considered are crossed by high temperature heat transfer fluid passing into storage and the same or another heat transfer fluid recovering high temperature heat from storage.

The contributions to installed cost fall into two categories:

- Variable costs that are determined by the capacity of storage chosen (i.e. the reactant inventory and the storage volumes for the reactants)
- Fixed costs that are determined by the thermal power level of operation specified (e.g. the ammonia synthesis reactors and other process items)

In addition to assessing the overall cost of storage capacity at the target size of 220 MW$_t$, with 6 hours of storage, we examine the relationship between installed cost per unit capacity and hours of storage and in the limit the “marginal” cost of adding extra storage capacity.

Variable costs can be measured directly in the units of \$/kWh$_t$ of installed storage capacity. Fixed costs are best quantified in units of \$/kW$_t$ of output capacity such that they can be subsequently divided by the hours of storage and placed on the same basis as variable costs.

To a large extent the cost of fixed cost items could be expected to be based on the established ammonia synthesis industry. Surveying available literature confirmed a view that the industry tends to hold cost information confidential. The information that is available refers to the development costs of complete plants (such as the Incitec Pivot 2013 Louisiana ammonia plant). Such information is of limited use as the majority of the cost is related to the preparation of the hydrogen and nitrogen feed gas via the reforming of natural gas.

Of the information available, the most directly applicable cost information was provided by the previous ANU system study [38] that was carried out in collaboration with the well-known Swiss ammonia system design company Ammonia Casale (now Casale SA). In addition to this there are a range of sources given that allow chemical process engineering systems to be cost estimated component by component and these have also been applied.

In this section, we present cost estimates of the ammonia TCES system, considering each of the following major components:

- Reactors: heat recovery, adiabatic, and autothermal
- Recuperating heat exchanger
- Compressor
- Chilled separator
- Physical storage of gases (underground)

Typical process design and development strategies in the chemical industry involve various stages of technical studies with increasing complexity (i.e., bench scale, pilot plant, detailed, optimized plant design). Capital cost estimates of increasing detail and accuracy also accompany these technical studies. Details about these capital cost methods can be found in several Process Development and Design textbooks [39-41].

Order of magnitude estimates are often based on bench scale data and a block flowsheet with the major pieces of equipment [39-41], and have an accuracy of ±50%. Module costs are estimated from published data that relate equipment characteristics (e.g., heat exchange area, reactor volume, pump duty) to purchased costs for standard processing equipment. These initial cost estimates are then adjusted by factors that account for differences in operating conditions (i.e., temperature and pressure) and material cost. They are also updated to the current year using a cost index.

This project has produced a process design for an ammonia-based thermochemical energy storage (ammonia TCES) system that is based on lab-scale data, a model developed from fundamental engineering design equations, and initial optimization studies. These inputs are similar to what an industrial company would use during development of a new process. Thus, the capital cost estimation methods used in the chemical processing industry (described above) are appropriate to estimate the cost of the plant design for this project.

ANU's 1997 study

This 1997 study considered a 1500 metric ton per day ammonia plant corresponding to a thermal output of 68.1 MW_t. The AUD costs from this study have been scaled to meet the conditions of the present study as shown in Table 6.

Table 6: Synthesis System Costs from 1997 ANU Study [38]

Subsystem	Reported Cost AUD	Cost USD	Specific fixed cost, $/kW$_t$	Specific cost in 2016, $/kW$_t$	Specific cost at 220 MW_t, $/kW$_t$	Specific cost after 4th plant, $/kW$_t$
Synthesis reactor	$5,100,000	$3,825,000	56.2	78.91	55.51	35.53
Gas compressor	$2,900,000	$2,175,000	31.9	44.87	31.56	20.20
Other equipment	$5,300,000	$3,975,000	58.4	82.01	57.69	36.92
TOTAL	**$13,300,000**	**$9,975,000**	**146.5**	**205.8**	**144.8**	**92.6**

The "Other equipment" category includes the key items of the recuperating heat exchanger and the chilled separator.

AUD has been converted to USD at a rate of 0.75. Costs in 2016 have been calculated using the ratio of the values of the chemical plant cost index [42], i.e. 386.5 in 1997 compared to 543 in 2015. The specific cost has been adjusted to a value for a 220 MW_t system, using the generally accepted principle of total plant cost increasing with capacity using an exponent of 0.7, (see for example [43]) with specific cost

consequently decreasing. Finally, the 1997 study calculated a first of a kind "non-optimized" system cost. A projection of cost reductions with number of plants completed was offered, consistent with the commonly used learning curve approach, where empirically, new energy technologies reduce in cost by around 20% with each doubling of deployment. A value obtainable after a fourth plant is offered as a reasonable basis for comparison to the Sunshot target. The final total specific cost of \$92.6/kW_t, if applied to a plant with 6 hours of storage, would contribute \$15.4/kWh_t of installed storage capacity. The ANU study discusses the potential for further cost reductions from incorporation of passive rather than active cooling of reactants to ambient temperature, however no allowance has been made for that at this point.

Reactors and Recuperating Heat Exchanger

The reactors have been modeled throughout this project as multiple tube-in-tube configurations, although it is intended that these would be realized as bundles of tubes running through a catalyst-filled shell. Essentially the reactors are heat exchangers with the addition of catalyst.

For comparison with the ANU system study, we have estimated their costs (along with the recuperating heat exchanger) using the methodology for shell and tube heat exchangers. Seider et al. [39], Peters et al. [40], and Smith [41] all provide cost estimation models for shell and tube heat exchangers. Their models are each correlated in terms of heat transfer area (based on the outer surface area of the tubes) for a base-case design, with various correction factors to account for deviations from the base-case design. The models can all be written as:

$$C_p = C_B(A) \times F_P \times F_M \times F_{other} \times I_1/I_0 \quad (9)$$

where C_P is the purchase cost, C_B is the cost of the base-case design as a function of area, F_P is a pressure factor to account for pressure different from atmospheric, F_M is a material factor to account for material other than carbon steel, F_{other} represents other factors that differ for the different models, and I_1 and I_0 are the cost indices in the current year and year of the base-case design respectively. Under the category of other correction factors, Seider et al. include a length factor and Smith uses a temperature factor.

The pressures and the high end temperatures reached and the presence of supercritical steam suggest a requirement for the use of high nickel content alloys such as Inconel in some portions of the system. This material has a considerably higher material cost factor than carbon steels. While this project has not attempted detailed engineering of full-sized reactors, there is a concept whereby an ammonia synthesis reactor is housed within a pressure vessel which has internal insulation. This has been used since the earliest days of the industry [43]. This means that vessel volume will be slightly increased but provides the benefit that the vessel walls can operate at much lower temperatures and thus can be fabricated from lower cost carbon steels. The assumption made here is that this approach would be followed and so the heat exchanger based cost estimation has been applied without the large material cost factors associated with Inconel.

Table 7 compares the results from the ANU study with the heat exchanger based empirical cost correlations from each of the sources. The value for the recuperating heat exchanger attributed to the ANU study is an estimated fraction of the total allocated to Other equipment above.

Table 7: Reactor and Heat Exchanger Cost Estimates

Subsystem	ANU	Seider	Smith	Peters	Average
Fixed costs	$/kW	$/kW	$/kW	$/kW	$/kW
Reactors	35.53	12.42	31.50	8.99	**22.11**
Recuperating Heat Exchanger	17.41	13.86	27.70	9.31	**17.07**

Within the accuracy of such estimations, there is reasonable consistency between the sources. The average values have been taken as the basis for further discussion noting that the range of accuracy is around ± 50%. It is reasonable that the estimated costs of reactors based on our design come out somewhat lower than the ANU study value, since our design has been optimized for heat recovery rather than ammonia production.

Incorporated within each of the reactor cost totals is a relatively small contribution from catalyst cost. The total volume of catalyst needed is 7.3 m^3; based on a value of 25 $/kg [44] the cost of the catalyst is $184,000.

Compressor

In a conventional ammonia plant, gas compressors are a major part of the capital cost and energy consumption. This is a consequence of the very large pressure difference between the pressures of natural gas supply and steam reformer operation and the high pressures needed for the ammonia synthesis reactor. For a closed loop system, the level of compression needed is linked to the difference in pressure between the reactant gas storage system and the ammonia synthesis reactor.

As has been noted, underground storage solutions typically employ a cushion gas equal to 30%, thus pressure may swing between 10 and 30 MPa. Thus in the case of close to fully depleted storage the compression ratio needed is only three compared to around 30 in a conventional ammonia plant. This considerably reduces the complexity and cost of a compressor. In the best case, if the pressure swing can be limited to a range in which the synthesizer can also operate, no compression at all would be needed other than to overcome the flow related pressure drop. Use of salt cavern based storage offers sufficiently cheap large volumes that this approach appears plausible in that case.

The Seider and Smith references offer correlations for compressor cost as a function of power requirement. Compressor costs based on a peak power requirement of 34 MW, arising from an assumed 10 MPa pressure increase, are compared with the number from the ANU study in Table 8. The assumption is that a compressor capable of a 10 MPa pressure boost at the specific volume of gas at 30 MPa would allow operation of the reactor at a nominal pressure of 30 MPa while allowing the storage to swing between 20 MPa and 40 MPa. There is considerable variation between the Seider and Smith numbers, nonetheless they are of the same order of magnitude and also similar to the ANU study result. Again they have been simply averaged.

Table 8: Compressor Cost Estimates

Subsystem	ANU	Seider	Smith	Average
Fixed costs	$/kW	$/kW	$/kW	$/kW
Compressor	20.20	48.33	22.72	**27.86**

Chilled separator

The chilled separator is the one aspect for which other sources of analysis have not been carried out. A value of \$19.5/kW_t has been assumed based on the ANU study, with the estimated recuperator cost subtracted from the "Other equipment" subtotal.

Storage of gases underground

As discussed earlier, solution mined salt caverns are favored as the lowest cost storage option. The sources consulted suggest that storage volumes could be achieved for \$1/kWh_t at 20 MPa and allowing for 33% buffer gas. To cover the contingencies of higher costs for what would be a smaller cavern by the standards of that industry and also allow for a further reduction in pressure swing, a figure of \$1.5/ kWh_t has been allowed.

The shaft drilling option which can offer greater site choice flexibility offers costs that translate to an energy storage specific cost of \$4.83/kWh_t if no buffer gas is required, rising to \$7.20/kWh_t if 33% buffer is allowed. The latter figure has been used as the more conservative and in any case operating with no buffer gas would add considerably to the cost and energy requirements for compression.

The inventory of reactants is assumed to be provided as an initial supply of ammonia at industry standard prices. The price of ammonia has been less than \$0.8/kg in the last few years at large volumes [45]; at 3.92 MJ/kg, this translates to \$0.73/kWh_t. For the case of salt cavern storage, this has been doubled to \$1.50/ kWh_t to allow for reduced pressure swing. For a shaft drilled system, it has been increased approximately 33% to \$1/kWh_t to allow for a smaller level of buffer gas.

Avoided cost of boiler

In comparing the ammonia TCES system with the default of a two tank molten salt system and the Sunshot cost target, it can be noted that this energy storage system eliminates the need for the boiler heat exchanger as it heats the steam in the synthesis reactor directly. As a result, a separate steam generating heat exchanger is not required (as it is with a molten salt based storage, for example). Thus the equivalent cost of such a heat exchanger can effectively be counted as a credit to the overall capital cost of ammonia-based TCES.

Boiler heat exchanger cost has been estimated from [42]. This source indicates that a boiler heat-exchanger for a system with 280 MW_t capacity is \$7.4 million, a specific cost of \$26.4/kW_t.

Overall assessment

The overall estimated cost of a 220 MW_t system with 6 hours of storage is summarized in Table 9, where the fixed costs have been converted to $/kWh_t$. The resulting cost is \$13/kWh_t and \$18/kWh_t for the salt cavern and shaft drilling options, respectively. Thus, at 6 hours of storage the ammonia system has good prospects of meeting the Sunshot target.

Table 9: Fixed and Variable Costs of the Entire Ammonia-Based TCES System

Fixed costs	**$/kW$_t$**	**Cost for 6 hours $/kWh$_t$**	
Reactor	22.11	3.69	
Recuperating Heat Exchanger	17.07	2.85	
Compressor	27.86	4.64	
Chilled Separator plus other BOP	19.50	3.25	
Offset for boiler	-26.38	-4.40	
Variable Costs		**Salt Cavern**	**Shaft Drilling**
Underground Storage Volume		1.50	7.20
Ammonia inventory		1.50	1.00
Total		**13.0**	**18.2**

It is apparent from this analysis that the marginal cost of storage, being the sum of just the variable costs, is very low. Against this though, the fixed costs of installation are very close to the same as those of a molten salt plant. This means that the apparent advantage of the new technology is greater the more hours of storage are applied. The terms of reference for the ELEMENTS program mandate the use of 6 hours storage for the analysis against the \$15/kWh_t target. In many markets 6 hours of storage is indicative of the configuration that is at present likely to offer the highest IRR in operation. There are other markets however, where more hours of storage would be favored and this will increase over time as the deployment of midday PV generation erodes the value of energy during sun hours.

Thus, Figure 25 examines the dependency of overall specific cost of installed storage capacity versus storage hours. This adds the variable cost of storage to the fixed cost amortized over the number of storage hours applied. The fixed and variable costs for molten salt were taken from [42]. The heavy line widths for the estimated costs are intended to suggest the uncertainty in those costs.

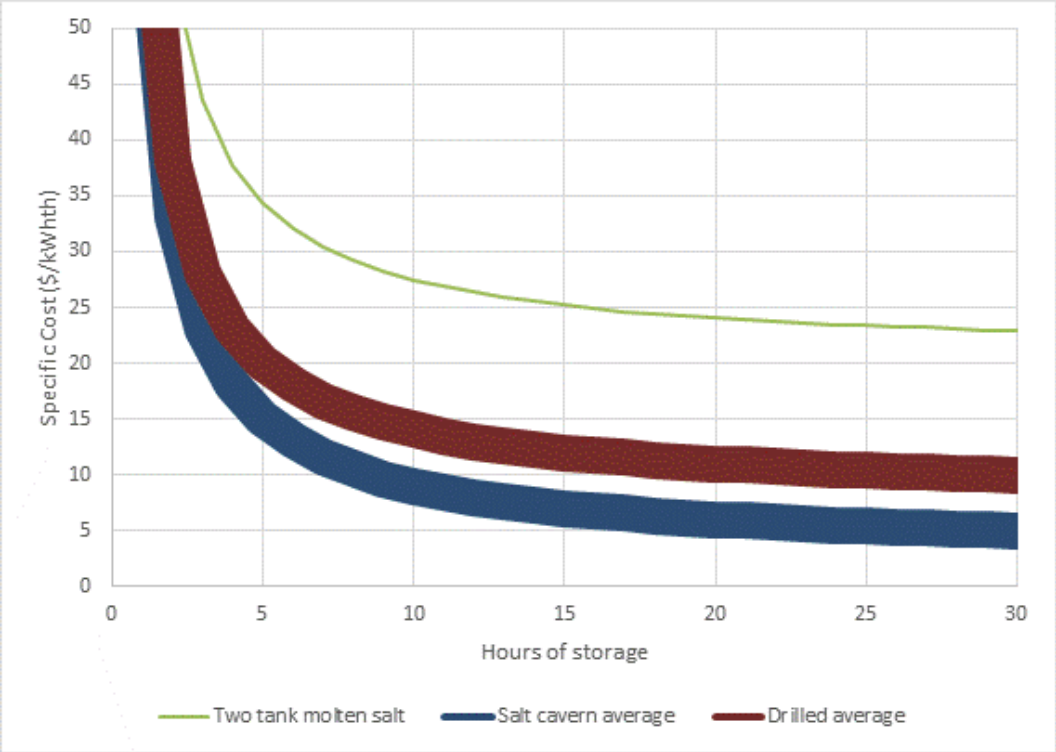

Figure 25: Cost of ammonia-based TCES system as a function of hours of storage.

As noted previously, at 6 hours of storage the ammonia system has good prospects of meeting the Sunshot target, especially for salt caverns. However, at 10 to 15 hours of storage, the effective cost of installed storage capacity drops well below the Sunshot target in both cases. The marginal cost of storage is sufficiently low in the case of a salt cavern based solution, that it suggests that the technology could be suited to offering storage sufficient to meet peak demands through several days of continuous cloud.

The greatest uncertainty with this cost analysis lies with the estimation of the fixed costs; it can be noted that even if these are doubled, the Sunshot target of $\$15/kWh_t$ would still be met at 10 hours of storage for the salt cavern option or 15 hours for drilled shaft systems.

CONCLUSIONS

The project has successfully demonstrated steam heating to 650°C and energy recovery to steam at the 5 kW_t level. We have identified two promising technologies for gas storage: salt caverns and drilled shafts. Together these two options answer the technical and economic challenge associated with storage of gas phase components. A conceptual design of an ammonia dissociation receiver has been developed that fits into the same size envelope as the molten salt receiver in SAM, has the same design thermal capacity, and has a calculated thermal efficiency of 94.6%. This establishes the technical feasibility of a surround field tower system using ammonia dissociation.

We have developed a modeling capability for ammonia synthesis reactors transferring heat to a secondary fluid, and have validated the model by comparison to our experimental data. A parametric study showed, among other things, the importance of

using small tube diameters and spacing to enhance heat transfer. Multi-parameter optimization was used to find a design that minimizes the wall material volume.

Finally, cost estimation has showed that the ammonia system has good prospects of meeting the Sunshot target: estimated costs of the entire synthesis system for the 220 MW_t plant with 6 hours of storage are \$13/kWh_t using salt cavern storage and \$18/kWh_t using shaft drilling. Costs per kWh_t are even lower with more hours of storage.

With the established technology of ammonia synthesis as a starting point, the successes of the project have mitigated technical risks associated with high-temperature synthesis reaction, underground storage, and tower receiver design. It is now possible to map a time line to commercial deployment that is likely to be shorter and less risky than other thermochemical cycles under active investigation.

All final deliverables have been achieved (as noted in the Introduction), as have the large majority of milestones. For brevity, only key Phase 2 milestones are summarized in the following table.

Major Task/Milestone Completion

SOPO Task # M.S. #	Task Title and Milestone Description	Successful?	Notes
T-2.3R	**Build a closed loop system consisting of dissociation, synthesis, and steam generator sub-systems.**		
M-2.3R	*It will be possible to supply N_2+3H_2 feed gas to the synthesis reactor at a rate up to 5 g/s, with pressures in the range 20 to 30 MPa and inlet temperatures between 500 and 600°C.*	*Yes.*	
T-5.1	**Run experiments for the purpose of improving and validating fundamental reaction and heat transfer behavior in the model.**		
M-5.1	*The results of model and experiments will agree to within 10% at the 95% confidence level. (Modified to base agreement on rms error.)*	*Yes.*	
T-5.2	**Conduct experiments on a sequence of more complex and larger scale reactor components for the purposes of model validation and demonstration of steam heating.**		
M-5.2	*The 5 kW_t reactor system will heat 2.5 g/s of steam from 350°C to an average value of 650°C under steady-state conditions, with 95% confidence.*	*Steam flow rate was 2.5 g/s and power to steam was 5.2 kW_t. Temperature rise was >300oC as desired, but starting at 335oC because of design flaw in steam generation system. Insufficient number of tests conducted on which to base statistical analysis.*	
T-5.3	**Continue Phase I Task 2.1 to perform preliminary testing of catalyst performance at 650°C.**		
M-5.3	*The decrease in ammonia yield will be less than 0.01 over the time span of the tests.*	*Yes.*	*No decrease in yield detected.*
T-6.1	**Use optimization tools to design a synthesis reactor system that will satisfy the utility-scale design specifications at minimum cost for the structural materials and catalyst.**		
M-6.1	*The cost of structural materials and catalyst, when added to the cost of underground storage, will achieve an overall cost for the thermochemical storage system of < \$15/kWh_t.*	*Yes.*	

BUDGET AND SCHEDULE

The project has ended on budget, having spent the DOE share of $1,182,788 and contributed the cost share of $295,800. The project began on 7/1/2014 and was granted a three-month no-cost extension because of the delay in continuing the funding at the start of Phase 2. The project ended on time on 9/30/2016, although admittedly we could have accomplished a more thorough investigation of the 5 kW_t system had we had more time.

PATH FORWARD

As well as successfully completing all the planned Tasks, this project has, in doing so, established that there are strong grounds to be optimistic that ammonia-based TCES will have a future role in commercial CSP systems.

Proving the ability to provide heat suitable for supercritical steam cycles is a major step forward. Interestingly, in the time that this project has been carried out, there is now increasing interest in the supercritical CO_2 cycle. It is apparent that the ammonia TCES system should also be applicable to that cycle and this is an area the team is keen to investigate.

In terms of continuing research, tasks that the group considers as immediate priorities for work, either in parallel or series, include:

- Continued operation and improvement to the 5 kW_t closed loop experiment.
- Upscaling to a solar driven closed loop using either one dish or an existing solar furnace research facility.
- Detailed techno-economic analysis of utility scale power plants using ammonia TCES with various levels of energy storage, including 30-40 hours.

The most critical aspect of the present work to the future commercial prospects is the identification of feasible and low cost approaches to storing the reactant gases underground. This completely removes the apparent disadvantage of a low energy density compared to solid phase TCES systems and converts the gas phase aspects to an advantage.

While the direct application of ammonia TCES to tower based CSP systems as targeted by the ELEMENTS program is appealing, there are other aspects that could add to the appeal and drive new areas of investigation.

There is strengthening interest in the use of ammonia as a fuel or hydrogen-carrying vector for transport or international trade. A proposal has been made by the group for internal UCLA funding to investigate this direction. In this context there are ideas for configuring CSP plants with ammonia TCES for power generation, in ways that allow the ammonia synthesis unit to be used for net ammonia production.

The trend to increasingly favor tower systems in the CSP industry is directly linked to the ability to effectively drive two-tank molten salt storage. Ammonia TCES has the flexibility of being potentially applicable to any concentrator solution. In the context of dishes, it can offer a means of collecting energy from large fields of dishes with no thermal loss from pipe networks, so opening up the potential to benefit from the

considerably higher optical efficiency capability. The linear concentrators, trough or Fresnel, also have the potential to drive ammonia-based TCES. Reactors would operate at lower temperature, however the phase separation abilities of ammonia TCES means that the recovery of heat at high temperatures would be unchanged, with the cycle effectively operated as a chemical heat pump. Thus the overall potential for application can be wider than molten salt.

Further serious progress will depend on developing commercial partnerships. As previously discussed, a full patent application has been filed (High Temperature Synthesis for Power Production and Storage, filed 6/27/2016, PCT/US2016/03964). Discussions have been initiated with potential investors that include a large high profile provider of industrial gases, an energy utility, and an international investment fund.

In an ideal scenario, the steps to full commercialization anticipated include:

1. Identification of partners – current to next 12 months
    - In parallel with continuation of experiments, modeling, and design and planning of solar-driven closed-loop experiment.
2. Solar-driven closed-loop test – 2017-2019
    - On sun, using existing tower-based test facility or single dish. Steam production but no power generation. Budget around $4 million.
3. Pilot 1 MW_e system – 2018-2021, followed by continuous operation
    - Gas storage fabricated above ground. Generate revenue from electricity sales sufficient to cover operating costs, operate for extended years as needed. Budget around $15 million.
4. First utility scale demonstration, 10 MW_e – 2019-2024, followed by continuous operation
    - First trial of underground storage using shaft drilling technology. Using off-the-shelf subcritical steam turbine. Significant financial assistance package required to build the first system, but operation and balance of financial package on fully commercial basis. Budget around $100 million.
5. First full-sized system, 100 MW_e, 10+ hrs storage – 2022-2027, followed by continuous operation
    - Underground storage either salt cavern or shaft drilled. Synthesis reactor produces supercritical steam at 650°C, potentially for a supercritical steam turbine. Preferential finance terms required, otherwise a fully commercial system. Budget around $700 million.

The University of California (UCLA) and IT Power are working together to identify partners to move to solar driven closed loop test and further identify the investment and partners needed for the subsequent steps.

REFERENCES

1. K.J. Albrecht, G.S. Jackson, and R.J. Braun, “Thermodynamically consistent modeling of redox-stable perovskite oxides for thermochemical energy conversion and storage,” *Applied Energy*, Vol. 165, pp. 285–296, 2016.
2. S.M. Babiniec, E.N. Coker, J.E. Miller, and A. Ambrosini, “Investigation of $La_xSr_{1-x}Co_yM_{1-y}O_{3-d}$ (M = Mn, Fe) perovskite materials as thermochemical energy storage media,” *Solar Energy*, Vol. 118, pp. 451-459, 2015.
3. E.C.E. Rönnebro, G. Whyatt, M. Powell, M. Westman, F.(R.) Zheng, Z.Z. Fang, “Metal Hydrides for High-Temperature Power Generation,” *Energies* Vol. 8, pp. 8406-8430; doi:10.3390/en8088406, 2015.
4. R.M. Melsert and S.K. Gangwal, “Calcium-Based Thermochemical Energy Storage System for use with High-Temperature Concentrating Solar Power Facilities,” extended abstract, SolarPACES 2015, Cape Town, South Africa.
5. N.R. Rhodes, A. Barde, K. Randhir, L. Li, D.W. Hahn, R. Mei, J.F. Klausner, and N. AuYeung, “Solar Thermochemical Energy Storage Through Carbonation Cycles of $SrCO_3$/SrO Supported on $SrZrO_3$,” ChemSusChem Vol. 8, pp. 3793 – 3798, 2015.
6. S.E. Nielsen, “Ammonia Synthesis: Catalyst and Technologies,” *Innovations in Industrial and Engineering Chemistry*, Chap. 2, pp.15-39, 2008.
7. N. Yahya, P. Puspitasari, K. Koziol, and P. Guiseppe, “Ammonia Synthesis,” in *Carbon and Oxide Nanostructures, Adv Struct Mater 5*, DOI 10.1007/8611_2010_25, # Springer-Verlag Berlin Heidelberg, 2010. Published online: 3 August, 2010.
8. R. Angira, “Simulation and Optimization of an Auto-Thermal Ammonia Synthesis Reactor,” *Int. J Chemical Reactor Engineering*, Vol. 9, Article A7, 2011.
9. S.R. Upreti and K. Deb, “Optimal Design of an Ammonia Synthesis Reactor Using Genetic Algorithms,” *Computers Chem. Engng,* Vol. 21, No. 1, pp. 87-92, 1997.
10. M. Pedernera, D.O. Borio, and J. A. Porras, “A New Cocurrent Reactor for Ammonia Synthesis,” *Chemical Engineering Science*, Vol. 51, No. 11, pp. 2927-2932, 1996.
11. K.A. Lovegrove, A. Luzzi, and H. Kreetz, “A solar-driven ammonia-based thermochemical energy storage system,” *Solar Energy*, Vol. 67, No. 4, pp. 309-316, 1999.
12. J. T. Richardson, et al., "Dynamics of a Sodium Heat Pipe Reforming Reactor," *AIChE Journal*, Vol. 34, pp. 743-752, May 1988.
13. H. Kreetz and K. Lovegrove, "Theoretical analysis and experimental results of a 1 kW(chem) ammonia synthesis reactor for a solar thermochemical energy storage system," *Solar Energy*, Vol. 67, pp. 287-296, 1999.
14. K. M. Lovegrove, "High pressure ammonia dissociation experiments for solar energy transport and storage," *International Journal of Energy Research*, Vol. 20, pp. 965-978, Nov 1996.
15. C. Chen, K. Lovegrove, H.P. Kavehpour, A.S. Lavine, “Design of an Ammonia Synthesis System for Producing Supercritical Steam in the Context of

Thermochemical Energy Storage," Proc. ASME Power Conf., Article No. V001T01A006, 2016.

16. J. R. Jennings, *Catalytic Ammonia Synthesis Fundamentals and Practice*, Plenum Press, NY, 1991.
17. J. Charles and G. Hill, *An Introduction to Chemical Engineering Kinetics and Reactor Design*, John Wiley & Sons, 1977.
18. T. H. Fletcher, et al., "Predicting the effectiveness factor for mth order Langmuir rate equations in spherical coordinates," *Abstracts of Papers of the American Chemical Society*, Vol. 218, pp. U641-U641, Aug 22 1999.
19. J. C. Dedeken, et al., "Steam Reforming of Natural-Gas—Intrinsic Kinetics, Diffusional Influences, and Reactor Design," *ACS Symposium Series*, Vol. 196, pp. 181-197, 1982.
20. ASME Boiler and Pressure Vessel Code
21. J. D. Jackson, "A Semi-Empirical Model of Turbulent Convective Heat Transfer to Fluids at Supercritical Pressure," *ICONE16: Proc. 16th Int'l Conf. Nuclear Engin.*, Vol 3, pp. 911-921, 2008.
22. S. Mokry, et al., "Development of supercritical water heat-transfer correlation for vertical bare tubes," *Nuclear Engineering and Design*, Vol. 241, pp. 1126-1136, Apr 2011.
23. K. Lovegrove and A. Luzzi, "Endothermic reactors for an ammonia based thermochemical solar energy storage and transport system," *Solar Energy*, Vol. 56, No. 4, pp. 361-371, 1996.
24. M. Panfilov, G. Gravier, and S. Fillacier, "Underground storage of H_2 and H_2-CO_2-CH_4 mixtures," *10th European Conference on the Mathematics of Oil Recovery*, 2006.
25. J. Apt et al., *An Engineering-Economic Analysis of Syngas Storage*, DOE/NETL-2008/1331, 2008.
26. C. Augustine et al., "A Comparison of Geothermal with Oil and Gas Well Drilling Costs," *Proc. Thirty-First Workshop on Geothermal Reservoir Engineering*, SGP-TR-179. 2006.
27. P. Chamley, ARUP Consulting, Tunneling discussion, 2008.
28. Z. Feng et al., *Vessel Design and Fabrication Technology for Stationary High-Pressure Hydrogen Storage*, ORNL, http://www.hydrogen.energy.gov/pdfs/review13/pd088_feng_2013_o.pdf, 2013.
29. G. Gill and G. Cowan, *Adavale Basin, Queensland Underground Salt Cavern Potential*, http://www.innovativeenergy.com.au/saltcavern/article%20for%20mining%20journal.pdf, 2008.
30. EIA, http://www.eia.gov/naturalgas/, 2008.
31. R.M. Dell and D.A.J. Rand, "Clean Energy," *Royal Society of Chemistry*, 2004.

32. J.B. Taylor et al., “Technical and economic assessment of methods for the storage of large quantities of hydrogen,” *International Journal of Hydrogen Energy*, Vol. 11, No. 1, pp. 5–22, 1986.

33. Innovative Energy Consulting Pty Ltd, “Boree Salt Gas Storage Development Project,” www.innovativeenergy.com.au, 2015.

34. T.L. Saaty, “Decision making with the analytic hierarchy process,” *International Journal of Services Sciences*, Vol. 1, No. 1, pp. 83-98, 2008.

35. D.L. Seibers and J.S. Kraabel, “Estimating Convective Energy Losses from Solar Central Receivers,” SAND84-8717, April 1984.

36. A.E. Sepulveda and L .Epstein, "The Repulsion Algorithm, a New Multistart Method for Global Optimization," *J of Structural Optimization*, Vol. 11, No. 3/4, June 1996, pp. 145-152.

37. K.S. Raju, *Fluid Mechanics, Heat Transfer, and Mass Transfer: Chemical Engineering Practice,* Wiley, Hoboken, 2011.

38. A. Luzzi, K. Lovegrove, E. Fillipi, H. Fricker, M. Schmitz-Goeb, M. Chandapillai, S. Kanef, “Base Load Solar Power Using the Haber Bosch Process,” Australian National University, Final report to Swiss Federal Office of Energy, Solar Chemistry and Hydrogen RD&D Program, 1997.

39. W. D. Seider, J. D. Seader, D. R. Lewin, S. Widago, *Product and Process Design Principles*, 3rd Edition, Wiley, 2009.

40. M. Peters, K. Timmerhaus, R. West, *Plant Design and Economics for Chemical Engineers*, 5th Edition, McGraw-Hill, 2003.

41. R. Smith, *Chemical Process Design and Integration*, Wiley, NY, 2005.

42. SAM costs molten salt power tower spreadsheet.

43. M. Appl, “Brief History of Ammonia Production,” *Nitrogen,* No. 100, British Sulphur Publishing (March-April 1976), p. 49, 1976.

44. Zauba Import Export Data, https://www.zauba.com/import-reforming-catalyst-hs-code.html.

45. Weekly Fertilizer Review, http://farmfutures.com/story-weekly-fertilizer-review-0-30765, 2013.